The Astrophysical Journal Supplement Series, 222:16 (22pp), 2016 February doi:10.3847/0067-0049/222/2/16

HERSCHEL OBSERVATIONS OF MAJOR MERGER PAIRS AT $z = 0$: DUST MASS AND STAR FORMATION

Chen Cao[1,2,3], Cong Kevin Xu[3], Donovan Domingue[4], Veronique Buat[5], Yi-Wen Cheng[6], Yu Gao[7], Jiasheng Huang[8], Thomas H. Jarrett[9], Ute Lisenfeld[10], Nanyao Lu[3], Joe Mazzarella[3], Wei-Hsin Sun[11], Hong Wu[12], Min S. Yun[13], Joseph Ronca[4], and Allison Jacques[4]

[1] School of Space Science and Physics, Shandong University, Weihai, Weihai, Shandong 264209, China; caochen@sdu.edu.cn
[2] Shandong Provincial Key Laboratory of Optical Astronomy & Solar-Terrestrial Environment, Weihai, Shandong 264209, China
[3] Infrared Processing and Analysis Center, California Institute of Technology 100-22, Pasadena, CA 91125, USA; cxu@ipac.caltech.edu
[4] Georgia College & State University, CBX 82, Milledgeville, GA 31061, USA
[5] Laboratoire d'Astrophysique de Marseille—LAM, Université d'Aix-Marseille & CNRS, UMR7326, 38 rue F. Joliot-Curie, F-13388 Marseille Cedex 13, France
[6] Institute of Astronomy, National Central University, Chung-Li 32054, Taiwan
[7] Purple Mountain Observatory, Chinese Academy of Sciences, 2 West Beijing Road, Nanjing 210008, China
[8] Harvard-Smithsonian Center for Astrophysics, 60 Garden Street, Cambridge, MA 02138, USA
[9] Astronomy Department, University of Cape Town, Rondebosch 7701, South Africa
[10] Departamento de Física Teórica y del Cosmos, Universidad de Granada, Spain
[11] Institute of Astrophysics, National Taiwan University and The National Museum of Natural Science, Taiwan
[12] National Astronomical Observatories, Chinese Academy of Sciences, Beijing, China
[13] Department of Astronomy, University of Massachusetts, Amherst, MA 01003, USA
Received 2015 September 7; accepted 2015 December 10; published 2016 February 10

ABSTRACT

We present *Herschel* PACS and SPIRE far-infrared (FIR) and submillimeter imaging observations for a large K-band selected sample of 88 close major-merger pairs of galaxies (H-KPAIRs) in 6 photometric bands (70, 100, 160, 250, 350, and 500 μm). Among 132 spiral galaxies in the 44 spiral–spiral (S+S) pairs and 44 spiral–elliptical (S+E) pairs, 113 are detected in at least 1 *Herschel* band. The star formation rate (SFR) and dust mass ($M_{\rm dust}$) are derived from the IR SED fitting. The mass of total gas ($M_{\rm gas}$) is estimated by assuming a constant dust-to-gas mass ratio of 0.01. Star-forming spiral galaxies (SFGs) in S+S pairs show significant enhancements in both specific star formation rate (sSFR) and star formation efficiency (SFE), while having nearly the same gas mass compared to control galaxies. On the other hand, for SFGs in S+E pairs, there is no significant sSFR enhancement and the mean SFE enhancement is significantly lower than that of SFGs in S+S pairs. This suggests an important role for the disk–disk collision in the interaction-induced star formation. The $M_{\rm gas}$ of SFGs in S+E pairs is marginally lower than that of their counterparts in both S+S pairs and the control sample. Paired galaxies with and without interaction signs do not differ significantly in their mean sSFR and SFE. As found in previous works, this much larger sample confirms that the primary and secondary spirals in S+S pairs follow a Holmberg effect correlation on sSFR.

Key words: galaxies: evolution – galaxies: general – galaxies: interactions – galaxies: starburst

Supporting material: figure set, machine-readable tables

1. INTRODUCTION

Galaxy interactions and mergers are important external mechanisms for triggering galactic evolution (Kormendy & Kennicutt 2004). Both observations and numerical simulations have shown that dynamical instabilities induced by galaxy interactions can cause cold gas inflow and massive star formation in the central region of disk galaxies (see, e.g., Bahcall et al. 1995; Dasyra et al. 2006; Hopkins et al. 2006). Merger-induced star formation was first predicted by Toomre & Toomre (1972) and confirmed by Larson & Tinsley (1978) in a study of optical colors of Arp galaxies. Many subsequent studies of the H_α emission and Far-infrared (FIR) emission in Arp galaxies and in paired galaxies provided further support of this theory (see Kennicutt 1996 for a review). On the other hand, Haynes & Herter (1988) found little or no enhanced FIR emission in a sample of optically selected pairs compared to a control sample of single galaxies. In a more influential paper, Bergvall et al. (2003) reported a multi-wavelength study in which they found no significant star formation rate (SFR) enhancement for a sample of morphologically selected merger candidates. Apparently, only some merging galaxies have significantly enhanced SFR, with ultra-luminous infrared galaxies (ULIRGs) as the extreme examples, and the others do not. Therefore, whether the mean SFR of a merger sample shows significant enhancement depends very much on how it is selected. Kennicutt et al. (1987) and Bushouse et al. (1988) found that merger candidates that show strong signs of tidal interactions have significantly stronger SFR enhancement than optically selected paired galaxies, the latter being only marginally enhanced (a factor of ~2) compared to single galaxies. Telesco et al. (1988) found a strong tendency for pairs with the highest FIR color temperatures to have the smallest separation. Xu & Sulentic (1991) showed that the enhancement of the FIR emission of close spiral–spiral (S+S) pairs with separation less than the size of the primary and with signs of interaction is significantly stronger than that of wider pairs and pairs without interaction signs. Sulentic (1989) found that elliptical–elliptical (E+E) pairs are equally quiet in the FIR emission as single ellipticals. Very few E's in S+E pairs are FIR bright, possibly cross-fueled by their S companions (Domingue et al. 2003).

More recently, large digitized surveys (e.g., SDSS, 2MASS, 2df, etc.) enabled large and homogeneously selected pair samples. A clear anti-correlation between the specific SFR (sSFR = SFR/$M_{\rm star}$) and the pair separation has been well

established (Barton et al. 2000; Lambas et al. 2003; Alonso et al. 2004; Nikolic et al. 2004; Ellison et al. 2008; Li et al. 2008; Scudder et al. 2012; Patton et al. 2013). In particular, close pairs with projected separation $r_{\rm proj} \leqslant 20\,h^{-1}$ kpc have relatively strong sSFR enhancement of a factor of $\gtrsim$2 (Ellison et al. 2008), while the sSFR enhancement of wider pairs is significantly weaker (Scudder et al. 2012; Patton et al. 2013). On the other hand, not all star-forming galaxies (SFGs) in close pairs have enhanced sSFRs. Xu et al. (2010) studied the sSFR enhancement in a sample of K-band-selected close major-merger pairs (primary-to-secondary mass ratio $m_{\rm pri}/m_{\rm 2nd} \leqslant 2.5$) using *Spitzer* FIR observations and found that (1) on average, SFGs in S+E pairs do not show any sSFR enhancement compared to their counterparts in a mass-matched control sample; and (2) the sSFR enhancement in S+S major-merger pairs is mass dependent in the sense that significant sSFR enhancement is confined to massive SFGs while no enhancement is found in low-mass SFGs with nearly equal (low) mass companions. Using data obtained in *Herschel* (PEP/HerMES) and *Spitzer* surveys of the COSMOS field (Scoville et al. 2007), Xu et al. (2012a) studied the cosmic evolution of the sSFR enhancement in close major-merger pairs since $z = 1$, and found that the sSFR enhancement in massive S+S pairs decreases with increasing redshift, while there is no significant sSFR enhancement in massive S+E pairs at any redshift. Other authors also found evidence for the lack of SFR enhancement in S+E pairs (Hwang et al. 2011; Moon & Yoon 2015) or low SFR activity in spiral galaxies with early-type close neighbors (Park & Choi 2005, 2009; Park et al. 2008). The literature results on the sSFR enhancement in close minor-merger pairs are controversial. Woods & Geller (2007) found that in close minor mergers, only secondary companions are sSFR enhanced, while there is no significant enhancement in primary companions. This is the opposite of the results of Lambas et al. (2003) that show stronger sSFR enhancement in the primaries. More recently, Scudder et al. (2012) found that both the primaries and the secondaries have significantly enhanced sSFRs in close minor-merger pairs. Lanz et al. (2013) studied SEDs for 31 interacting galaxies in 14 major and minor-merger systems, and found increases in SFR but not sSFR as the interaction sequences progress from non-interacting to strongly interacting.

In this paper, we present new FIR imaging observations in the six photometry bands (70, 100, 160, 250, 350, and 500 μm) of *Herschel* PACS (Poglitsch et al. 2010) and SPIRE (Griffin et al. 2010), for a large and complete sample of close major-merger pairs of SFGs (including both S+S and S+E pairs). The focus of this new study is on the dependence of the SFR enhancement on the dust mass, which is a good proxy of gas mass. Star formation activity in galaxies is fueled by cold gas, which dominates the gas mass, and all SFGs are gas-rich. Does the SFR enhancement depend on the gas content of a paired SFG? Both in simulations (Hopkins et al. 2009; Perret et al. 2014; Scudder et al. 2015) and in observations (Xu et al. 2012a) there have been indications that the SFR enhancement may decrease with increasing gas fraction. According to Hopkins et al. (2009) (see also Mihos & Hernquist 1996), this is because the gravitational torque imposed by the stellar disk on the gas disk is less effective when the gas fraction is high, therefore less disk gas can sink to the nuclear region to fuel the merger-induced starburst by losing angular momentum to stars. Maps of the dust emission in the six *Herschel* bands enabled us to accurately estimate the dust mass (and its distribution) for individual SFGs. All galaxies in our *Herschel* sample, a subset of the KPAIR sample of K-band selected major-merger pairs (Domingue et al. 2009; Xu et al. 2012b), have $M_{\rm star} > 10^{10}\,M_{\odot}$ and normal metallicity. Therefore their gas mass is likely to be related to dust mass with a rather constant gas-to-dust ratio of ~100 (Draine & Li 2007), and the sSFR versus $M_{\rm gas}$ relation for these paired SFGs can be explored using the *Herschel* observations. It is worth noting that it is difficult to directly measure the gas mass in individual galaxies in close major-merger pairs. The angular resolutions of single-dish HI 21 cm line observations are too coarse (beam $\gtrsim 5'$) to resolve pairs into individual galaxies, while the interferometry observations using the VLA are very expensive in terms of the integration time.

The rest of the paper is arranged as follows. Section 2 describes the selection of the H-KPAIR sample, and the details of the *Herschel* observation and photometry are given in Section 3. Section 4 shows the images and catalogs of the H-KPAIR galaxies and describes the estimation of dust mass and SFRs using SED fittings, while we describe the selection, data reduction, and photometry on control sample galaxies in Section 5. Sections 6 and 7 show statistical comparison results on sSFRs, total gas masses, and star formation efficiencies (SFEs) in H-KPAIRs and the control sample. Discussions will be given in Section 8. We summarize our results and briefly introduce future plans in Section 9.

Throughout this paper, we adopt the Λ-cosmology with $\Omega_{\rm m} = 0.3$ and $\Omega_{\Lambda} = 0.7$, and $H_0 = 70$ (km s^{-1} Mpc^{-1}).

2. THE *Herschel* KPAIR (H-KPAIR) SAMPLE

The local galaxy pairs sample used in this work (hereafter *Herschel* KPAIR sample, or H-KPAIR) was constructed from the KPAIR, which is a complete and unbiased K-band selected sample of 170 close major-merger galaxy pairs (see details in Domingue et al. 2009; Xu et al. 2010). Pairs in the KPAIR with the following characteristics are excluded from H-KPAIR: (1) Elliptical+Elliptical (E+E) pairs; (2) pairs with only one measured redshift; (3) pairs with recession velocities $<$2000 km s^{-1}. The resulting sample contains 88 galaxy pairs (176 paired galaxies), of which 44 are Spiral+Spiral (S+S) pairs and 44 are Spiral+Elliptical (S+E) pairs. The interaction morphology of these pairs was visually checked by three of us (C. C., C. K. X., and D. D). Accordingly, pairs are classified into three types: (1) INT (with signs of interacting, e.g., morphological distortions, tidal tails and bridges, plumes etc.), (2) MER (merging systems) and (3) JUS ("just" pairs without clear signs of interaction). All galaxies have $z < 0.1$, with a median of $z = 0.04$.

3. *Herschel* OBSERVATIONS

3.1. PACS and SPIRE Images

Pairs in H-KPAIR were observed successfully using PACS and SPIRE photometers in the three PACS bands (70, 100, 160 μm) and three SPIRE bands (250, 350, 500 μm). The observations of 83 pairs were carried out within our own proposal (OT2_cxu_2). All but two of these pairs are smaller than 2′, while the sizes of two large pairs (J1406+5043 and J2047+0019) are between 3′ and 5′.

PACS observations were done in the scanmap mode with medium scan speed (20″/s). Each pair was observed with four

Table 1
H-KPAIR Galaxy Sample

(1) Pair ID (KPAIR)	(2) Galaxy ID (2MASX)	(3) R.A. (J2000)	(4) decl. (J2000)	(5) z redshift	(6) K_s (mag)	(7) Type	(8) Int-type	(9) *Herschel*-ID	(10) s(p) (kpc)	(11) δ(Vz) (km s^{-1})
J0020+0049	J00202580+0049350	5.107446	0.826346	0.014864	10.98	S	JUS	OT2_cxu_2	11.44	402.0
	J00202748+0050009	5.114637	0.833554	0.016204	10.5	E	JUS			
J0118−0013	J01183417−0013416	19.642259	−0.228261	0.045344	12.05	S	JUS	OT2_cxu_2	27.23	54.0
	J01183556−0013594	19.648352	−0.233075	0.045524	12.88	S	JUS			
J0211−0039	J02110638−0039191	32.776675	−0.655108	0.017746	11.42	S	JUS	OT2_cxu_2	10.63	96.0
	J02110832−0039171	32.784577	−0.654777	0.018066	10.9	S	JUS			
J0338+0109	J03381222+0110088	54.550919	1.16912	0.039201	12.42	S	INT	OT2_cxu_2	24.9	432.9
	J03381299+0109414	54.554136	1.161523	0.040644	12.77	E	INT			
J0754+1648	J07543194+1648214	118.633109	16.805959	0.045869	12.03	S	MER	OT2_cxu_2	13.89	104.1
	J07543221+1648349	118.634232	16.809722	0.046216	11.55	S	MER			
J0808+3854	J08083377+3854534	122.14073	38.914841	0.040173	12.37	S	JUS	OT2_cxu_2	18.71	23.7
	J08083563+3854522	122.148487	38.914504	0.040094	11.88	E	JUS			
J0823+2120	J08233266+2120171	125.886114	21.338096	0.018076	12.15	S	JUS	OT2_cxu_2	15.44	0.3
	J08233421+2120515	125.892554	21.34764	0.018075	11.52	S	JUS			
J0829+5531	J08291491+5531227	127.312147	55.522992	0.025059	11.73	S	JUS	OT2_cxu_2	27.75	55.2
	J08292083+5531081	127.336797	55.518931	0.025243	11.42	S	JUS			
J0836+4722	J08364482+4722188	129.186777	47.371907	0.05256	12.28	S	JUS	OT2_cxu_2	15.8	0.0
	J08364588+4722100	129.191208	47.369469	0.05256	11.9	S	JUS			
J0838+3054	J08381759+3054534	129.573312	30.914861	0.047559	12.65	S	INT	OT2_cxu_2	9.09	152.7
	J08381795+3055011	129.5748	30.916973	0.048068	11.94	S	INT			
J0839+3613	J08385973+3613164	129.748888	36.221234	0.055618	12.04	E	JUS	OT2_cxu_2	26.58	231.6
	J08390125+3613042	129.755226	36.217846	0.054846	12.55	S	JUS			
J0841+2642	J08414959+2642578	130.456662	26.716073	0.084834	12.27	S	JUS	OT2_cxu_2	30.64	300.0
	J08415054+2642475	130.460609	26.713209	0.085834	12.99	E	JUS			
J0906+5144	J09060283+5144411	136.511812	51.744702	0.02912	11.68	E	JUS	OT2_cxu_2	24.29	3.3
	J09060498+5144071	136.520782	51.735305	0.029131	11.95	S	JUS			
J0912+3547	J09123636+3547180	138.151523	35.788345	0.023532	11.53	E	JUS	OT2_cxu_2	14.24	6.0
	J09123676+3547462	138.153186	35.796182	0.023512	12.34	S	JUS			
J0913+4742	J09134461+4742165	138.435884	47.704599	0.051226	11.91	E	INT	OT2_cxu_2	24.32	450.9
	J09134606+4742001	138.441955	47.700051	0.052729	12.1	S	INT			
J0915+4419	J09155467+4419510	138.977827	44.33086	0.039568	12.23	S	MER	OT1_dsanders_1	9.69	2.4
	J09155552+4419580	138.981364	44.332785	0.039576	11.31	S	MER			
J0926+0447	J09264111+0447247	141.671319	4.790211	0.089132	13.16	S	MER	OT2_cxu_2	8.13	483.6
	J09264137+0447260	141.672412	4.790559	0.090744	12.48	S	MER			
J0937+0245	J09374413+0245394	144.433951	2.760819	0.024156	10.01	S	INT	OT2_cxu_2	25.64	197.7
	J09374506+0244504	144.437634	2.74737	0.023497	10.45	E	INT			
J1010+5440	J10100079+5440198	152.503332	54.672181	0.046004	12.2	S	MER	OT2_cxu_2	13.92	83.7
	J10100212+5440279	152.508859	54.674434	0.046283	12.34	S	MER			
J1015+0657	J10155257+0657330	153.969058	6.959172	0.029931	12.28	S	JUS	OT2_cxu_2	13.02	244.5
	J10155338+0657495	153.972451	6.963758	0.029116	11.3	E	JUS			
J1020+4831	J10205188+4831096	155.216286	48.519406	0.052968	13.26	S	INT	OT2_cxu_2	25.94	45.0
	J10205369+4831246	155.223658	48.523383	0.053118	12.27	E	INT			
J1022+3446	J10225647+3446564	155.73532	34.78235	0.05537	13.18	S	INT	OT2_cxu_2	11.56	301.5
	J10225655+3446468	155.735626	34.779681	0.056375	12.39	S	INT			
J1023+4220	J10233658+4220477	155.902453	42.346583	0.045621	12.36	S	INT	OT2_cxu_2	15.98	53.1
	J10233684+4221037	155.903524	42.351041	0.045444	13.01	S	INT			
J1027+0114	J10272950+0114490	156.872904	1.246742	0.023592	11.79	S	INT	OT2_cxu_2	14.21	64.8
	J10272970+0115170	156.873782	1.254605	0.023376	10.9	E	INT			
J1032+5306	J10325316+5306536	158.22153	53.114916	0.06403	12.62	S	INT	OT2_cxu_2	8.32	44.7
	J10325321+5306477	158.221747	53.113263	0.063881	12.15	E	INT			
J1033+4404	J10332972+4404342	158.373843	44.076176	0.052303	11.91	S	JUS	OT2_cxu_2	27.42	64.2
	J10333162+4404212	158.381778	44.072572	0.052089	12.37	S	JUS			
J1036+5447	J10364274+5447356	159.178124	54.79323	0.045841	12.47	S	INT	OT2_cxu_2	16.9	17.1
	J10364400+5447489	159.183338	54.796929	0.045784	11.63	E	INT			
J1039+3904	J10392338+3904501	159.847442	39.080611	0.043464	12.49	S	JUS	OT2_cxu_2	20.35	43.2
	J10392515+3904573	159.854824	39.082589	0.04332	12.29	E	JUS			
J1043+0645	J10435053+0645466	160.960666	6.76296	0.028694	11.96	S	INT	OT2_cxu_2	23.23	173.7
	J10435268+0645256	160.969501	6.75702	0.028115	12.2	S	INT			
J1045+3910	J10452478+3910298	161.353285	39.174955	0.026834	11.63	S	JUS	OT2_cxu_2	22.72	340.5
	J10452496+3909499	161.354008	39.163873	0.025699	11.41	E	JUS			
J1051+5101	J10514368+5101195	162.93181	51.022155	0.025027	10.27	E	JUS	OT2_cxu_2	6.99	366.0
	J10514450+5101303	162.935331	51.025075	0.023807	10.97	S	JUS			

Table 1
(Continued)

(1) Pair ID (KPAIR)	(2) Galaxy ID (2MASX)	(3) R.A. (J2000)	(4) decl. (J2000)	(5) z redshift	(6) K_s (mag)	(7) Type	(8) Int-type	(9) *Herschel*-ID	(10) s(p) (kpc)	(11) δ(Vz) (km s^{-1})
J1059+0857	J10595869+0857215	164.994547	8.955983	0.063163	12.01	E	JUS	OT2_cxu_2	21.62	140.1
	J10595915+0857357	164.996465	8.95992	0.062696	12.95	S	JUS			
J1101+5720	J11014357+5720058	165.431565	57.334969	0.046903	12.46	E	JUS	KPGT_soliver_1	28.03	276.0
	J11014364+5720336	165.431837	57.342686	0.047823	13.17	S	JUS			
J1106+4751	J11064944+4751119	166.706021	47.853312	0.064324	12.66	S	INT	OT2_cxu_2	17.92	334.8
	J11065068+4751090	166.711183	47.85252	0.06544	12.44	S	INT			
J1120+0028	J11204657+0028142	170.194061	0.470612	0.025534	11.78	S	JUS	OT2_cxu_2	12.33	25.2
	J11204801+0028068	170.200062	0.468579	0.025618	11.0	S	JUS			
J1125+0226	J11251704+0227007	171.321025	2.450198	0.050379	12.75	S	INT	OT2_cxu_2	12.99	84.0
	J11251716+0226488	171.321518	2.446913	0.050659	12.14	S	INT			
J1127+3604	J11273289+3604168	171.887066	36.071335	0.035053	11.67	S	JUS	OT2_cxu_2	27.43	25.2
	J11273467+3603470	171.894471	36.063083	0.035137	10.82	S	JUS			
J1137+4728	J11375476+4727588	174.478176	47.466349	0.034334	11.28	E	JUS	OT2_cxu_2	26.63	137.7
	J11375801+4728143	174.491711	47.470652	0.033875	11.86	S	JUS			
J1144+3332	J11440335+3332062	176.013986	33.535072	0.031799	11.74	E	INT	OT2_cxu_2	20.48	100.5
	J11440433+3332339	176.018049	33.54277	0.031464	12.66	S	INT			
J1148+3547	J11484370+3547002	177.182095	35.783414	0.064099	12.81	S	INT	OT2_cxu_2	29.11	144.0
	J11484525+3547092	177.188549	35.785896	0.063619	11.94	S	INT			
J1150+3746	J11501333+3746107	177.555564	37.769659	0.055042	12.7	S	INT	OT2_cxu_2	25.36	149.4
	J11501399+3746306	177.558293	37.775167	0.05554	12.44	S	INT			
J1150+1444	J11505764+1444200	177.740186	14.738912	0.057202	12.69	S	INT	OT2_cxu_2	17.17	300.0
	J11505844+1444124	177.743517	14.736805	0.056202	11.73	E	INT			
J1154+4932	J11542299+4932509	178.595801	49.547493	0.070154	13.0	S	INT	OT2_cxu_2	8.23	308.4
	J11542307+4932456	178.596149	49.546019	0.071182	12.02	E	INT			
J1202+5342	J12020424+5342317	180.517927	53.708769	0.064651	12.97	S	INT	OT2_cxu_2	27.14	210.3
	J12020537+5342487	180.522233	53.713478	0.06395	12.43	E	INT			
J1205+0135	J12054066+0135365	181.419422	1.59349	0.022002	12.1	S	JUS	OT2_cxu_2	30.83	332.4
	J12054073+0134302	181.419711	1.575058	0.020894	11.21	E	JUS			
J1211+4039	J12115507+4039182	182.97949	40.655067	0.022854	11.82	S	INT	OT2_cxu_2	7.73	195.3
	J12115648+4039184	182.98535	40.655124	0.023505	11.98	S	INT			
J1219+1201	J12191719+1200582	184.821646	12.01619	0.027303	11.83	E	INT	OT2_cxu_2	13.18	160.8
	J12191866+1201054	184.827781	12.018189	0.026767	12.8	S	INT			
J1243+4405	J12433887+4405399	190.911978	44.094436	0.041791	12.09	S	JUS	OT2_cxu_2	22.6	249.9
	J12433936+4406046	190.914009	44.101295	0.040958	11.94	E	JUS			
J1252+4645	J12525011+4645272	193.208797	46.757577	0.061331	12.42	S	JUS	OT2_cxu_2	27.67	104.7
	J12525212+4645294	193.21717	46.758185	0.060982	12.2	E	JUS			
J1301+4803	J13011662+4803366	195.319279	48.06018	0.030278	12.2	S	INT	OT2_cxu_2	11.84	129.6
	J13011835+4803304	195.326491	48.058471	0.029846	12.67	S	INT			
J1308+0422	J13082737+0422125	197.114112	4.370179	0.025476	13.39	S	JUS	OT2_cxu_2	18.52	66.0
	J13082964+0422045	197.123418	4.367971	0.025696	12.44	S	JUS			
J1313+3910	J13131429+3910360	198.309546	39.176686	0.071586	12.24	E	INT	OT2_cxu_2	8.29	0.0
	J13131470+3910382	198.311265	39.177305	0.071586	13.1	S	INT			
J1315+4424	J13151386+4424264	198.807791	44.407356	0.03586	12.01	S	INT	OT1_rmushotz_1	27.84	35.1
	J13151726+4424255	198.821937	44.407105	0.035743	11.23	S	INT			
J1315+6207	J13153076+6207447	198.878026	62.129135	0.030566	11.99	S	INT	OT1_dsanders_1	22.39	6.0
	J13153506+6207287	198.896085	62.124613	0.030586	11.54	S	INT			
J1332−0301	J13325525−0301347	203.230301	−3.026349	0.049306	12.95	S	INT	OT2_cxu_2	21.45	297.0
	J13325655−0301395	203.235759	−3.027679	0.048316	12.19	S	INT			
J1346−0325	J13462001−0325407	206.583483	−3.428114	0.024781	11.19	S	JUS	OT2_cxu_2	25.03	222.0
	J13462215−0325057	206.592397	−3.418283	0.025521	11.66	E	JUS			
J1400−0254	J14003661−0254327	210.152556	−2.909102	0.025579	11.49	S	INT	OT2_cxu_2	12.23	391.5
	J14003796−0254227	210.15818	−2.906313	0.026884	11.73	S	INT			
J1400+4251	J14005783+4251203	210.240969	42.85566	0.032741	11.87	S	INT	OT2_cxu_2	27.27	234.3
	J14005879+4250427	210.244986	42.845198	0.033522	12.18	S	INT			
J1405+6542	J14055079+6542598	211.461632	65.716632	0.03063	12.8	S	JUS	OT2_cxu_2	23.27	39.6
	J14055334+6542277	211.472286	65.707721	0.030762	12.0	E	JUS			
J1406+5043	J14062157+5043303	211.589913	50.725106	0.006456	9.7	S	JUS	OT2_cxu_2	25.21	240.6
	J14064127+5043239	211.671969	50.723327	0.007258	9.56	E	JUS			
J1407−0234	J14070703−0234513	211.779296	−2.580923	0.058555	12.44	S	INT	OT2_cxu_2	14.43	300.0
	J14070720−0234402	211.780016	−2.577849	0.057555	12.96	E	INT			
J1423+3400	J14234238+3400324	215.926602	34.009016	0.013553	11.48	S	JUS	OT2_cxu_2	16.14	294.0
	J14234632+3401012	215.943004	34.017002	0.012573	11.04	S	JUS			

Table 1
(Continued)

(1) Pair ID (KPAIR)	(2) Galaxy ID (2MASX)	(3) R.A. (J2000)	(4) decl. (J2000)	(5) z redshift	(6) K_s (mag)	(7) Type	(8) Int-type	(9) *Herschel*-ID	(10) s(p) (kpc)	(11) δ(Vz) (km s^{-1})
J1424−0304	J14245831−0303597	216.242996	−3.066606	0.052517	12.37	S	JUS	OT2_cxu_2	13.91	300.0
	J14245913−0304012	216.246381	−3.067027	0.053517	11.9	S	JUS			
J1425+0313	J14250552+0313590	216.272925	3.233119	0.037083	11.98	E	INT	OT2_cxu_2	22.37	114.0
	J14250739+0313560	216.280712	3.232055	0.037463	12.97	S	INT			
J1429+3534	J14294766+3534275	217.448585	35.574313	0.028996	10.93	S	JUS	KPGT_soliver_1	22.07	180.3
	J14295031+3534122	217.459663	35.570065	0.029597	11.9	S	JUS			
J1433+4004	J14334683+4004512	218.445139	40.080911	0.026047	10.78	S	INT	OT2_cxu_2	28.01	114.0
	J14334840+4005392	218.451475	40.094155	0.026427	11.17	S	INT			
J1444+1207	J14442055+1207429	221.085649	12.128593	0.030445	11.51	S	MER	OT2_cxu_2	8.26	299.4
	J14442079+1207552	221.086655	12.132	0.031443	10.72	S	MER			
J1500+4317	J15002374+4316559	225.098935	43.282197	0.031088	11.34	E	JUS	OT2_cxu_2	14.58	147.0
	J15002500+4317131	225.10417	43.286997	0.031578	11.73	S	JUS			
J1505+3427	J15053137+3427534	226.380709	34.464851	0.074528	12.98	S	INT	OT2_cxu_2	9.55	300.0
	J15053183+3427526	226.38266	34.464635	0.073528	12.36	E	INT			
J1506+0346	J15064391+0346364	226.682879	3.776844	0.036278	11.48	S	JUS	OT2_cxu_2	25.24	315.0
	J15064579+0346214	226.690883	3.772574	0.035228	11.6	S	JUS			
J1510+5810	J15101587+5810425	227.566059	58.178518	0.030343	11.77	S	JUS	OT2_cxu_2	10.54	402.0
	J15101776+5810375	227.574164	58.176979	0.031683	12.35	S	JUS			
J1514+0403	J15144544+0403587	228.689368	4.06633	0.0386	11.89	S	INT	OT2_cxu_2	18.81	186.0
	J15144697+0403576	228.695709	4.066007	0.03922	12.06	S	INT			
J1523+3748	J15233768+3749030	230.907038	37.817522	0.023365	12.55	S	INT	OT2_cxu_2	20.09	78.3
	J15233899+3748254	230.912489	37.807073	0.023626	12.43	E	INT			
J1526+5915	J15264774+5915464	231.698953	59.262907	0.044712	12.45	S	INT	OT2_cxu_2	8.77	224.1
	J15264892+5915478	231.703856	59.263304	0.045459	12.13	E	INT			
J1528+4255	J15281276+4255474	232.053241	42.929924	0.018839	10.02	S	INT	OT2_cxu_2	26.53	243.0
	J15281667+4256384	232.069607	42.944107	0.018029	10.59	S	INT			
J1552+4620	J15523258+4620180	238.135769	46.338356	0.059385	12.07	E	INT	OT2_cxu_2	19.46	489.0
	J15523393+4620237	238.141398	46.339933	0.061015	12.75	S	INT			
J1556+4757	J15562191+4757172	239.091225	47.954829	0.019103	12.1	S	JUS	OT2_cxu_2	22.96	240.0
	J15562738+4757302	239.114264	47.958429	0.019903	12.16	E	JUS			
J1558+3227	J15583749+3227379	239.656243	32.460535	0.049368	13.16	S	INT	OT2_cxu_2	10.8	261.0
	J15583784+3227471	239.657667	32.463088	0.048498	12.29	S	INT			
J1602+4111	J16024254+4111499	240.677392	41.197267	0.033536	11.69	S	JUS	OT2_cxu_2	18.66	69.0
	J16024475+4111589	240.686475	41.199706	0.033306	12.5	S	JUS			
J1608+2529	J16080559+2529091	242.023328	25.485866	0.041547	11.94	S	MER	OT2_cxu_2	10.96	224.1
	J16080648+2529066	242.02704	25.485182	0.042294	11.32	S	MER			
J1608+2328	J16082261+2328459	242.094219	23.479425	0.04092	13.17	S	JUS	OT2_cxu_2	22.25	31.8
	J16082354+2328240	242.098125	23.473347	0.040814	12.44	S	JUS			
J1614+3711	J16145418+3711064	243.72577	37.185123	0.058169	12.13	S	INT	OT2_cxu_2	9.13	0.0
	J16145421+3711136	243.725893	37.187131	0.058169	12.04	E	INT			
J1628+4109	J16282497+4110064	247.104069	41.168463	0.033017	11.47	S	JUS	OT2_cxu_2	27.9	370.8
	J16282756+4109395	247.114849	41.161	0.031781	11.52	S	JUS			
J1635+2630	J16354293+2630494	248.928908	26.513727	0.070061	12.29	S	INT	OT2_cxu_2	14.99	378.0
	J16354366+2630505	248.931925	26.514045	0.071321	12.22	E	INT			
J1637+4650	J16372583+4650161	249.357631	46.837824	0.057817	11.8	S	JUS	OT2_cxu_2	25.82	299.7
	J16372754+4650054	249.364787	46.834858	0.056818	12.44	S	JUS			
J1702+1859	J17020320+1900006	255.513366	19.000181	0.057322	12.39	E	INT	OT2_cxu_2	17.14	462.6
	J17020378+1859495	255.515763	18.997088	0.05578	13.18	S	INT			
J1704+3448	J17045089+3448530	256.212001	34.814721	0.057213	13.06	S	INT	OT2_cxu_2	11.74	270.0
	J17045097+3449020	256.212288	34.817342	0.056313	12.4	S	INT			
J2047+0019	J20471908+0019150	311.829434	0.320801	0.012971	9.08	S	JUS	OT2_cxu_2	28.98	414.0
	J20472428+0018030	311.851263	0.300826	0.011591	9.74	E	JUS			

Note. Descriptions of columns: (1) Pair ID. The designations are "KPAIR J0020+0049," etc. (2) Galaxy ID, taken from 2MASS. (3) R.A. (deg, J2000). (4) decl. (deg, J2000). (5) redshift z taken from SDSS or other telescopes. (6) $K_{\rm rms}$ (K_{20}) magnitude taken from 2MASS. (7) Morphological type (S: Spirals, E: Ellipticals). (8) Interacting morphological type (INT: with interaction signs; MER: mergers; JUS: without interacting signs, "just" pairs). (9) *Herschel* proposal ID. (10) Projected separation (s(p)) between two galaxies in pairs, in kpc. (11) The difference in radial velocity (δ(Vz)) between two galaxies in pairs, in km s^{-1}.

(This table is available in machine-readable form.)

concatenated PACS observations. The first two are for the 70 and 160 μm bands with orientation angles of +45° (nominal) and −45° (orthogonal), respectively, and the other two are for the 100 and 160 μm bands of the same cross-scan configuration. For small pairs (<2′), each scan map has six scans with separation of 30″ and scan length = 3. This yields nearly

uniform coverage of a $3' \times 3'$ region, leaving enough margins outside the pairs for background determination. The average 4σ sensitivity limits are 36, 42, and 56 mJy for the three PACS bands. For large pairs we used scan number = 10, separation = $36''$, and scan length = $6'$, yielding a uniform coverage of a $6' \times 6'$ region and the average 4σ sensitivity limits of 30, 36, and 48 mJy. Data reduction was carried out using the *Herschel* Interactive Processing Environment (HIPE; Ott 2010), with the mapmaking done using UNIMAP (Traficante et al. 2011). The mean beam size (FWHM) are $5\farcs7$, $6\farcs8$, and $12\farcs0$ for 70, 100, and 1600 μm images, respectively.

SPIRE observations of small pairs were done in the small-map mode, providing uniformly covered cross-scan maps of $4' \times 4'$ in 3 SPIRE bands. For large pairs, the observations were done in the large-map mode with nominal scan speed ($30''$/s), both scan length and scan height equal to $6'$, and in the A and B directions. For both the small and large maps, each observation has 4 repeats, yielding confusion limited 4σ sensitivities of 29, 30, and 34 mJy in the 3 SPIRE bands, respectively. The SPIRE data were reduced using HIPE 10.0.0, which uses the de-striper for the mapmaking. Bad pixels (PSWF8, PSWE9, PSWB5, PSWD11) were masked. The mean beam FWHM are $18\farcs2$, $24\farcs9$, and $36\farcs3$ for 250, 350, and 500 μm images, respectively.

The remaining 5 pairs in H-KPAIR were observed by other OT and KPGT projects, and their *Herschel* data were taken from the archives. SPIRE images of two pairs (J1101+5720 and J1429+3534) were taken directly from HerMES data release v2. In Table 1 we present the pair and galaxy ID, R.A., and decl., redshift (z), Ks-band magnitude (from 2MASS), morphological types (spiral or elliptical), interaction morphological types (as described in Section 2), and *Herschel* proposal ID for 176 paired galaxies in the H-KPAIR sample. SDSS, PACS, and SPIRE images of all pairs are shown in Figure 1.

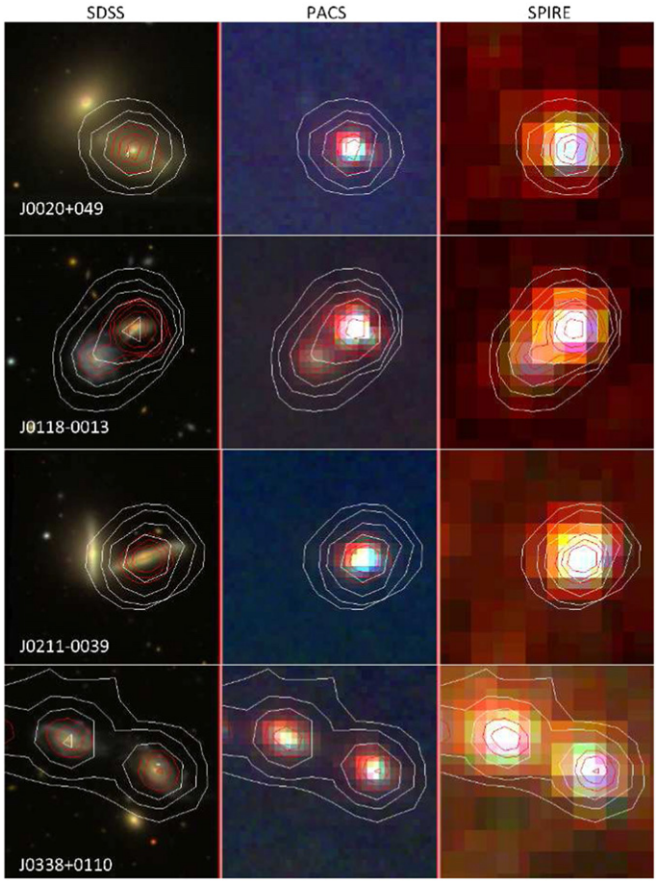

Figure 1. SDSS, *Herschel* PACS, and SPIRE three-color images of H-KPAIR galaxy pairs. All images are overlaid by the same two sets of contours of 70 μm (red) and 250 μm (white) images.

(The complete figure set (22 images) is available.)

3.2. PACS and SPIRE Photometry

We made extended-source photometry on individual galaxies in each pair to get their integrated FIR-submillimeter fluxes. The following two methods were used.

1. *Aperture photometry*: for pairs with large separation compared with the beam size of a given band, elliptical/circular apertures were selected and aperture photometry was performed. The photometric error is the quadratic sum of the background subtraction error and the rms error as calculated in Dale et al. (2012). For PACS data, photometry in aperture matching annuli were used to determine the values for sky background subtraction. For SPIRE data, the sky background was estimated using the mean of photometric measurements on eight elliptical/circular regions (of the same size as the photometric aperture) surrounding the pair. Aperture corrections were applied according to measurements on the point-spread function (PSF) images.
2. *IMFIT model-fitting photometry*: for blended pairs with small separation, IMFIT (Erwin 2015) was used to do the two-component simultaneous model fitting to get the deblended flux for each galaxy. The PACS photometry simultaneously fits a combination of sky level, Gaussians, and exponential disks for both galaxy components. Initial parameters include the peak intensity, coordinates and appropriate scale. The IMFIT uses χ^2 minimization and the residual images were examined and adjusted manually. Subsequent initial parameter adjustments were performed to minimize the residual images. The relative flux of each galaxy is fairly robust to the parameter adjustments. Total aperture flux of the pair with division based on relative fits was therefore the chosen photometric method. Errors are based on the area-dependent background error estimation for this large aperture, with a conservative approach based on half the area of the flux assigned to each galaxy. The pair J0926+0447 is too blended for the fits to converge to a useful residual and the relative flux could not be determined. The reported errors for this pair are large, but constrained by the total flux. The SPIRE photometry uses two types of models in IMFIT: (1) PSF model for point-like galaxies; (2) two-dimensional (2D) Gaussian for extended galaxies. Both models also include an uniform background. The photometric errors were estimated using the rms error measured on the residual images: $\text{error}_{\text{rms}}$ = rms (residual,per pixel) $\times N/\sqrt{n}$ (N: number of pixels in the aperture; n: number of beams in the aperture).

Color corrections were made for 3 SPIRE bands with multiplicative correcting factors of 0.95385, 0.95632, 0.97215 for 250, 350, 500 μm fluxes, respectively. No calibration errors

are included in the PACS and SPIRE photometric errors. Upper limits of 4σ were given for non-detections in both the aperture and model-fitting photometry methods.

4. DUST MASS, $L_{\rm IR}$, AND STELLAR MASS

The dust mass $M_{\rm dust}$ and integrated infrared luminosity $L_{\rm IR}$ (8–1000 μm) of individual galaxies are estimated via FIR-submillimeter spectral energy distribution (SED) fitting using the dust emission model of Draine & Li (2007; hereafter DL07). The DL07 model includes emissions from polycyclic aromatic hydrocarbon (PAH) molecules and graphite and silicate grains, covering the entire IR wavelength range from the mid-infrared (MIR) through the submillimeter. It is consistent with observations of a variety of infrared continuum and PAH features in local galaxies (e.g., Draine et al. 2007; see also Dale et al. 2012 for more detailed descriptions). In the SED fittings, the Milky way extinction curve (MW3.1) is assumed and the maximum interstellar radiation field intensity is fixed at Umax $= 10^6$. The best-fit values of parameters $M_{\rm dust}$, gamma, qPAH (between 0.5 and 4.5 with the step of 0.1), and Umin (among values of 0.10, 0.15, 0.20, 0.30, 0.40, 0.50, 0.70, 0.80, 1.00, 1.20, 1.50, 2.00, 2.50, 3.00, 4.00, 5.00, 7.00, 8.00, 12.0, 15.0, 20.0, and 25.0) are then found via a simple χ^2 minimization. The errors of $M_{\rm dust}$ include two terms: (1) error associated with model fitting, estimated using Bayesian analysis (da Cunha et al. 2008); and (2) error caused by observational uncertainties, estimated using a Monte-Carlo method: it equals to the standard deviation of the values of $M_{\rm dust}$ resulting from fittings of 300 simulated IR-submillimeter SEDs. In each SED, the flux in a given *Herschel* band is generated randomly, assuming a Gaussian probability distribution with the mean equal to the observed flux and the σ equal to the photometric error. The mean errors of $M_{\rm dust}$ for spirals in H-KPAIRs are estimated to be: 0.086 ± 0.020 dex ($\log_{10}(M_\odot)$), 0.101 ± 0.044 dex, and 0.213 ± 0.191 dex for those with all 6-band *Herschel* detections, 5-band *Herschel* detections, and 4-band *Herschel* detections, respectively.

We carried out a test to check whether the lack of MIR broadband fluxes in the SED fittings introduces any bias, using ~25 H-KPAIR spirals observed by *Spitzer* (Xu et al. 2010). As shown in Figure 2, the $M_{\rm dust}$ obtained using SED fittings with and without MIR fluxes (IRAC 8 and MIPS 24 μm) agrees very well with each other. The scatter is quite small and much lower than other uncertainties. We also found good agreement between $L_{\rm IR}$ and $L_{\rm TIR}$ (estimated from 24, 70, 160 μm luminosities; Dale et al. 2005). Thus, both the $M_{\rm dust}$ and $L_{\rm IR}$ estimated using the DL07model SED fittings from FIR-submillimeter bands are reliable even though the MIR data points are missing. On the other hand, in trials that used the two-graybody model (2GB; Dunne & Eales 2001) in the SED fittings of H-KPAIR galaxies, we found that the resulting $M_{\rm dust}$ and $L_{\rm IR}$ are both systematically lower than those obtained using the DL07model (Figure 3). This is mainly due to the fact that the 2 GB model does not include the MIR emission at $\lambda < 20$ μm; therefore it underestimates $M_{\rm dust}$ and $L_{\rm IR}$ (Dale et al. 2012).

It should be noted that there might be a systematic underestimation (up to 20%) of the $L_{\rm IR}$ for galaxies with very warm MIR-to-FIR colors ($f(25\,\mu{\rm m})/f(60\,\mu{\rm m}) > 0.2$). These sources are generally associated with bright active galactic nuclei (AGNs; Surace et al. 1998). As discussed in Section 8.1, very few galaxies in our samples may be associated with bright AGNs. Therefore our results shall not be affected significantly by this possible bias. Indeed, Figure 4 shows the dependence of $L_{\rm IR}$ estimations using DL07 SED fittings without or with MIR (*Spitzer* IRAC and MIPS 24 μm) data points on *Spitzer* MIR-to-FIR colors: $f(24\,\mu{\rm m})/f(70\,\mu{\rm m})$, for 30 spirals in H-KPAIRs that were also included in Xu et al. (2010). There is only one spiral in pairs (J20471908+0019150) with warm MIR-to-FIR color ($f(24\,\mu{\rm m})/f(70\,\mu{\rm m}) > 0.2$), and there are no obvious underestimations of $L_{\rm IR}$ without the use of MIR points.

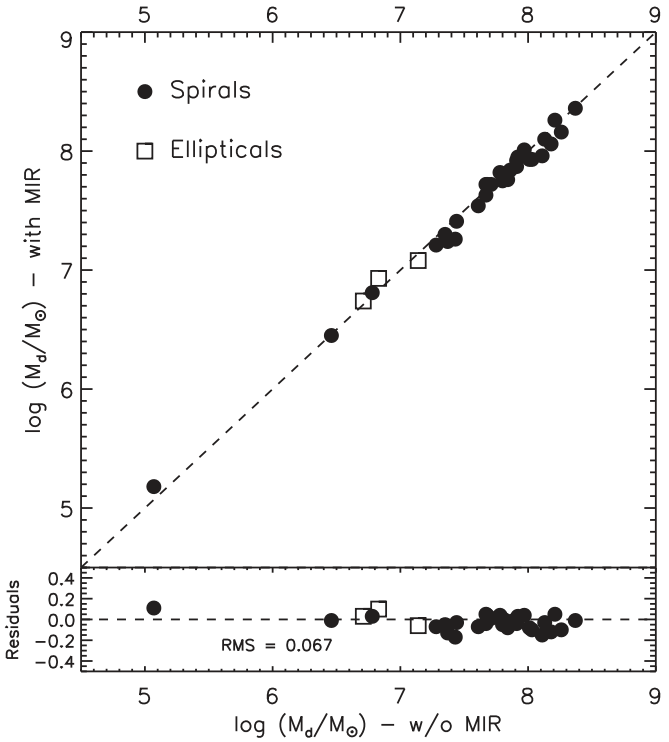

Figure 2. Comparison of dust masses using the DL07SED fitting with and without MIR fluxes for H-KPAIR galaxies with *Spitzer* observations by Xu et al. (2010). Spirals are shown as black dots and ellipticals are shown as open squares. Residuals are shown in the bottom panel.

For H-KPAIR and control sample galaxies (see Section 5) with a number of *Herschel* band of detections less than four, we used an empirical relation between $M_{\rm dust}$ and $L_{250\,\mu{\rm m}}$ (the monochromatic luminosity νL_ν at 250 μm) to estimate the dust mass (or its upper limit) from the 250 μm flux (or the upper limit). The adopted relation is $\log(M_{\rm dust}/M_\odot) = -0.13 + 0.83 \times \log(L_{250\,\mu{\rm m}}/L_\odot)$. The $L_{\rm IR}$ (or its upper-limit) of these galaxies was estimated from the the 100 μm flux (or the upper-limit) according to another empirical relation: $\log(L_{\rm IR}/L_\odot) = 0.84 + 0.95 \times \log(L_{100\,\mu{\rm m}}/L_\odot)$. Both relations were derived using H-KPAIR spirals with all 6-band or 5-band detections. Comparing results obtained from SED fittings to those calculated using these relations, the rms errors of the two empirical relations are 0.27 dex (for $M_{\rm dust}$) and 0.11 dex (for $L_{\rm IR}$), respectively.

In Tables 2 and 3 we listed the *Herschel* fluxes, stellar mass $M_{\rm star}$, the SFR, and total gas masses $M_{\rm gas}$ ($M_{\rm gas} = 100 \times M_{\rm dust}$) of paired spiral and elliptical galaxies, respectively. The SFR is derived from $L_{\rm IR}$ using the formula of Kennicutt (1998), with an additional correction factor of $10^{-0.20}$ for the conversion from the Salpeter IMF to the Kroupa IMF (Calzetti 2013). It is worth noting that this formalism misses the contribution from

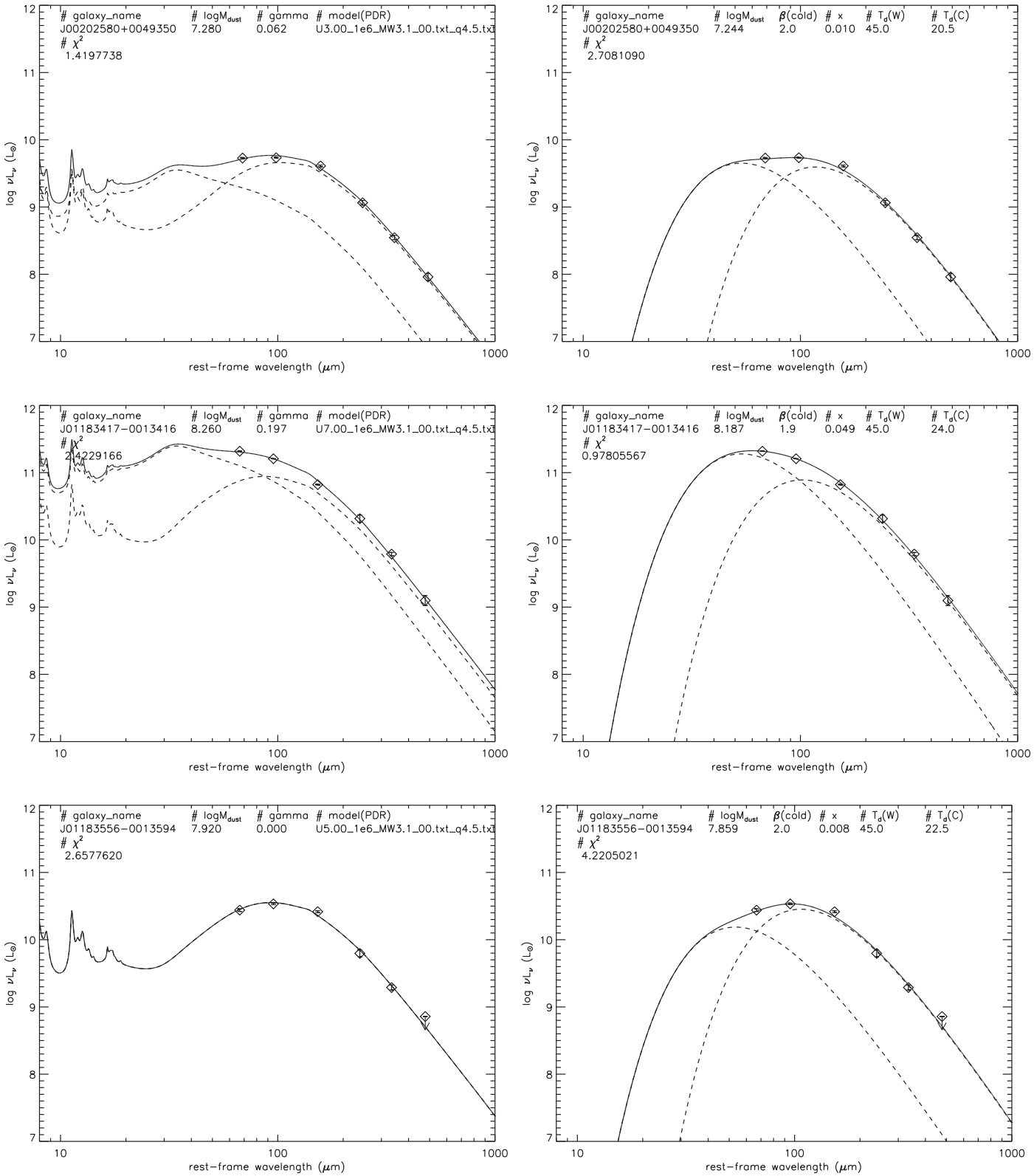

Figure 3. Examples of DL07 (left panels) and 2 GB (right panels) SED fittings for 3 spirals in H-KPAIR.

unobscured UV radiation, which is on the order of 20% for KPAIR galaxies (Yuan et al. 2012). It is also contaminated by the dust emission powered by the radiation of old stars (Buat & Xu 1996). However, since the same formalism is applied to both H-KPAIR galaxies and control galaxies, these possible biases shall not affect the results on the star formation enhancement of paired galaxies. $M_{\rm star}$ is estimated using 2MASS Ks band luminosity: $M_{\rm star}/L_{\rm K} = 1.32\ M_{\odot}/L_{\odot}$ (Xu et al. 2004; Domingue et al. 2009), with an additional correction factor of $10^{-0.39}$ (Xu et al. 2012b) in order to match

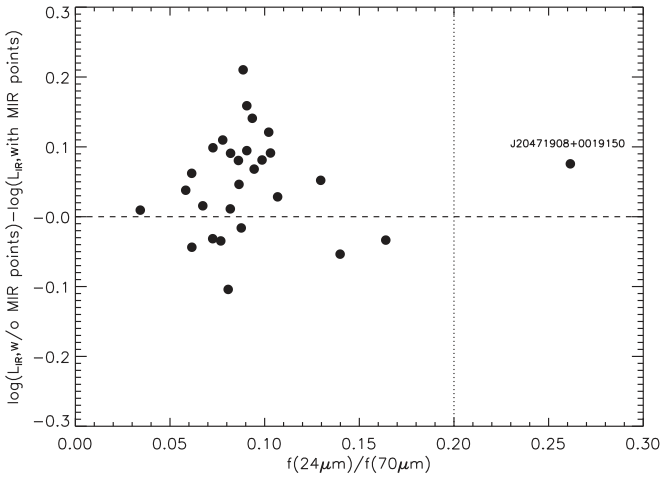

Figure 4. Differences between $L_{\rm IR}$ using the DL07SED fitting without and with MIR fluxes vs. MIR-to-FIR color: $f(24\ \mu{\rm m})/f(70\ \mu{\rm m})$, for H-KPAIR spiral galaxies with *Spitzer* observations by Xu et al. (2010).

those given in SDSS value-added catalogs (Kauffmann et al. 2003; with Kroupa IMF).

Chang et al. (2015) recently published stellar masses and SFRs for 1 M galaxies from SDSS+*WISE*, estimated based on 0.4 to 22 μm SEDs using the MAGPHYS (da Cunha et al. 2008) energy balance SED fitting technique. Chang et al.'s work also includes 85 spirals in pairs and all 132 spirals in controls in our samples. Comparisons of stellar masses and SFRs estimated in our work and in Chang et al. (2015) are shown in Figures 5 and 6, respectively.

From the comparisons, for most of the spirals with higher stellar masses, we found that using 2MASS Ks band luminosities (our work) and SED model fitting (Chang et al. 2015) will result in very similar $M_{\rm star}$ values. While this only applies for spirals with the lowest stellar masses, Chang et al. (2015) estimated lower $M_{\rm star}$ (∼0.3 dex) than ours. For comparison, for SFRs Chang et al.'s (2015) values are systematically lower than ours, especially for spirals in the control sample. This may be caused by: (1) in our work, larger beams of *Herschel* FIR-to-submillimeter bands resulting in more background contaminations; (2) in Chang et al. (2015), underestimation of dust obscurations for optical-to-MIR bands in MAGPHYS SED fittings; (3) the fact that the sizes of our local paired and control galaxies are generally much larger than the PSFs of SDSS and *WISE*, therefore, using MODELFLUX for SDSS 5-bands and PSF model flux for *WISE* 4-bands (although applied a correction using R_e) may still cause some flux loss in Chang et al. (2015), especially for the estimations of SFRs using *WISE* bands.

5. CONTROL SAMPLE

The control sample was selected among 2MASS galaxies of redshift $z < 0.1$ (from SDSS), found in four Level-5 HerMES fields: Bootes HerMES, EGS HerMES, ELAIS N1 HerMES, and Lockman SWIRE. Details of the *Herschel* PACS and SPIRE observations in these fields can be found in Oliver et al. (2012). The morphologies of these galaxies (S or E) were obtained from visual classifications by Galaxy Zoo (data release v1, Lintott et al. 2011). For those galaxies labeled "UNCERTAIN" in the Galaxy Zoo catalog, two of us (C. C. and C. K. X) visually re-classified them into S or E categories using SDSS optical images. For those galaxies with controversial classifications between us, we used an automatic classification algorithm described in Xu et al. (2010) ($u-r$ color and R_{50}/R_{90} ratio) as the third party. Then, close pairs (have companions with projected distance <70 kpc and $dM_{\rm star}$ <0.4 dex), peculiars (visually selected by C. C. and C. K. X.), and objects at the edge of PACS or SPIRE images (with low coverage) were rejected from the sample. The resulting parent control sample was then 1-to-1 matched with H-KPAIRs. The matched control galaxies have: (1) the same morphology (S or E); (2) similar stellar mass: $\delta M_{\rm star} < 0.1$ dex except for the match of J13082737+0422125, which is $\delta M_{\rm star} = 0.15$; (3) with the closest z to that of the corresponding H-KPAIR galaxy.

The *Herschel* PACS images at 100 and 160 μm (the 70 μm band was not included in the HerMES survey) and SPIRE images at 250, 350, 500 μm were taken from the HerMES data release (v2) for the 176 control sample galaxies. PACS and SPIRE aperture photometries were made using IDL/phot and circular apertures. Fixed circular aperture sizes were used for most galaxies, with aperture radii of 12″, 18″ for PACS 100 and 160 μm, and 24″, 33.″33, and 48″ for SPIRE 250, 350, and 500 μm, respectively. Larger apertures were used for a few extended galaxies. The background and error estimates are similar to those in the aperture photometry of H-KPAIR galaxies (Section 3). The total dust masses, SFRs and stellar masses of control sample galaxies were calculated using the same method as for the H-KPAIR galaxies (Section 4). In Table 4 we list the galaxy ID (name), R.A. and decl., redshifts, the *Herschel* fluxes, stellar mass $M_{\rm star}$, the SFR, and total gas masses $M_{\rm gas}$ ($M_{\rm gas} = 100 \times M_{\rm dust}$) of spiral galaxies in the control sample.

It should be noted in the following comparisonal analysis with the control sample, each galaxy in the pairs of our H-KPAIR sample was included independently, rather than the pair as whole, which would introduce a bias.

6. SPECIFIC SFR ENHANCEMENT

Figure 7 is a scatterplot for the relation between $M_{\rm star}$ and the sSFR for spirals in H-KPAIR and in the control sample. The maximum likelihood Kaplan–Meier (K–M) estimator (Kaplan & Meier 1958, see also Xu et al. 1998), which exploits information in the upper limits, was used to calculate the means of the sSFR of different populations. For spirals in H-KPAIR the mean is $\log({\rm sSFR/yr^{-1}}) = -10.66 \pm 0.06$, and for spirals in the control sample it is nearly identical: $\log({\rm sSFR/yr^{-1}}) = -10.65 \pm 0.04$. However, detailed inspections of Figure 7 reveal a mismatch between the H-KPAIR and the control sample: while none of the control galaxies have a value or upper limit of $\log({\rm sSFR/yr^{-1}})$ below −11.3, many H-KPAIR spirals have their $\log({\rm sSFR/yr^{-1}})$ values/upper limits below this threshold. This is due to the fact that control galaxies are more distant (median $z = 0.056$) than H-KPAIR galaxies (median $z = 0.040$), and their *Herschel* observations in the HerMES Level-5 survey (Oliver et al. 2012) are shallower than our H-KPAIR observations. Therefore their upper limits are in general significantly higher than those of H-KPAIR galaxies, and none of them were detected below $\log({\rm sSFR/yr^{-1}}) = -11.3$. This mismatch can bias the mean of the control sample toward higher values even though the K–M estimator is used, for the algorithm requires that the detections cover the entire data range and the detections and

Table 2
Herschel 6-Band Fluxes and Physical Parameters of H-KPAIR Spirals

(1) Galaxy ID (2MASX)	(2) F70 μm (mJy)	(3) F100 μm (mJy)	(4) F160 μm (mJy)	(5) P-PACS	(6) F250 μm (mJy)	(7) F350 μm (mJy)	(8) F500 μm (mJy)	(9) P-SPIRE	(10) log $M_{\rm star}$ ($M_\odot$)	(11) SFR ($M_\odot$ yr^{-1})	(12) log $M_{\rm gas}$ ($M_\odot$)
J00202580+0049350	738.90 ± 14.03	1067.90 ± 15.14	1288.50 ± 40.76	AAA	571.35 ± 46.82	242.06 ± 17.53	90.04 ± 11.28	APP	10.49	1.39	9.28
J01183417–0013416	3507.90 ± 20.73	3874.90 ± 22.54	2555.50 ± 33.61	MMM	1246.09 ± 163.57	517.78 ± 28.79	150.56 ± 28.41	PPP	10.98	55.91	10.26
J01183556–0013594	459.70 ± 20.73	814.30 ± 22.54	997.10 ± 33.61	MMM	373.62 ± 46.31	162.56 ± 14.32	<86.01	PPP	10.65	5.92	9.92
J02110638–0039191	1126.50 ± 15.75	1822.70 ± 17.70	1839.40 ± 51.51	AAA	989.35 ± 83.06	401.95 ± 20.05	135.12 ± 11.49	APP	10.45	2.95	9.61
J02110832–0039171	<37.65	<42.34	<60.49	AAA	52.50 ± 9.65	<25.81	<35.17	APP	10.68	<0.09	8.67
J03381222+0110088	368.04 ± 9.08	607.68 ± 9.90	801.85 ± 16.88	AAA	513.69 ± 47.72	200.00 ± 31.08	<92.45	APP	10.70	5.02	10.13
J07543194+1648214	1365.84 ± 10.40	1934.76 ± 11.60	2078.56 ± 29.24	MMM	1024.48 ± 50.21	361.63 ± 19.41	101.26 ± 21.93	PPP	10.96	18.00	10.22
J07543221+1648349	769.56 ± 10.40	1485.14 ± 11.60	1434.74 ± 29.24	MMM	790.32 ± 63.32	422.92 ± 16.90	167.38 ± 21.69	PPP	11.15	12.02	10.42
J08083377+3854534	121.91 ± 5.59	223.42 ± 6.56	167.75 ± 12.23	AAA	127.53 ± 15.64	63.36 ± 14.90	<51.08	PPP	10.71	1.35	9.36
J08233266+2120171	732.66 ± 7.06	1037.70 ± 11.49	928.07 ± 14.95	AAA	538.00 ± 42.87	193.89 ± 10.74	76.23 ± 12.43	AGP	10.08	1.71	9.26
J08233421+2120515	933.60 ± 8.62	1229.60 ± 16.68	1115.50 ± 21.58	AAA	643.17 ± 43.90	223.94 ± 22.02	83.05 ± 13.54	AGP	10.34	2.27	9.33
J08291491+5531227	344.84 ± 19.45	674.10 ± 17.78	957.97 ± 26.71	AAA	614.63 ± 45.86	295.64 ± 26.82	160.67 ± 9.75	AAG	10.56	1.93	10.06
J08292083+5531081	368.50 ± 12.42	697.51 ± 14.41	927.75 ± 19.50	AAA	691.67 ± 45.51	363.71 ± 28.46	120.42 ± 11.07	AAG	10.69	2.05	10.00
J08364482+4722188	43.04 ± 8.44	55.95 ± 8.26	69.16 ± 14.98	AAA	<65.06	<29.21	<37.30	PPP	10.98	0.82	<9.49
J08364588+4722100	<33.75	<33.05	<59.90	AAA	<35.67	<31.45	<30.70	PPP	11.13	<0.49	<9.27
J08381759+3054534	232.06 ± 5.87	365.96 ± 5.92	581.73 ± 12.75	MMM	137.05 ± 11.63	69.74 ± 10.84	<36.50	GPP	10.74	2.90	9.61
J08381795+3055011	91.52 ± 5.87	144.27 ± 5.92	<59.49	MMM	161.38 ± 11.29	77.64 ± 11.02	38.19 ± 8.99	GPP	11.03	1.31	8.28
J08390125+3613042	62.86 ± 8.09	104.81 ± 4.79	221.31 ± 14.71	AAA	161.63 ± 12.42	74.07 ± 12.79	33.46 ± 7.98	PPP	10.91	1.91	10.13
J08414959+2642578	25.88 ± 5.11	70.29 ± 8.46	106.84 ± 15.80	AAA	56.00 ± 8.24	<25.91	<33.25	PPP	11.41	1.44	9.69
J09060498+5144071	155.62 ± 8.21	270.74 ± 8.46	492.79 ± 20.23	AAA	338.81 ± 24.19	157.22 ± 16.16	69.62 ± 10.39	AAP	10.60	1.26	9.84
J09123676+3547462	<14.80	<13.55	<16.17	AAA	<28.35	<20.63	<41.44	PPP	10.24	<0.04	<8.57
J09134606+4742001	208.14 ± 10.16	406.01 ± 8.89	589.73 ± 21.83	AAA	308.54 ± 11.21	148.80 ± 8.83	62.91 ± 8.28	GGP	11.05	4.27	10.13
J09155467+4419510	2426.67 ± 14.10	2992.48 ± 12.48	2994.09 ± 28.97	MMM	1085.36 ± 92.00	342.20 ± 31.64	248.93 ± 27.21	PPP	10.74	26.18	10.19
J09155552+4419580	4541.43 ± 14.10	5820.14 ± 12.48	5134.21 ± 28.97	MMM	2254.33 ± 100.27	1026.76 ± 31.55	218.35 ± 26.69	PPP	11.11	43.22	10.41
J09264111+0447247	16.36 ± 16.36	19.36 ± 19.36	19.80 ± 19.80	CCC	37.60 ± 8.04	<36.87	<36.94	PPP	11.10	1.05	10.37
J09264137+0447260	16.36 ± 16.36	19.36 ± 19.36	19.80 ± 19.80	CCC	<35.49	<36.21	<36.72	PPP	11.38	0.91	<9.70
J09374413+0245394	2601.60 ± 38.65	4557.40 ± 45.05	6157.90 ± 78.87	AAA	3101.00 ± 124.44	1347.92 ± 77.60	505.41 ± 50.50	AAA	11.16	9.83	10.37
J10100079+5440198	427.64 ± 8.06	969.53 ± 7.00	1404.19 ± 26.20	MMM	735.36 ± 57.31	356.73 ± 22.99	123.55 ± 13.80	PPP	10.89	6.40	10.35
J10100212+5440279	168.22 ± 8.06	312.57 ± 7.00	430.61 ± 26.20	MMM	366.34 ± 40.03	128.19 ± 14.54	<57.69	PPP	10.84	3.30	10.08
J10155257+0657330	<15.62	64.94 ± 5.58	85.74 ± 7.00	AAA	95.76 ± 12.28	<51.46	<45.76	PPP	10.45	0.28	9.16
J10205188+4831096	138.95 ± 5.57	298.69 ± 9.27	290.63 ± 16.50	AAA	167.91 ± 13.07	70.55 ± 8.64	<34.74	PPP	10.59	2.10	9.67
J10225647+3446564	244.08 ± 6.22	332.40 ± 7.06	352.31 ± 18.98	AAA	176.55 ± 10.60	85.87 ± 8.87	42.32 ± 8.71	PPP	10.66	5.65	9.88
J10225655+3446468	<13.71	<15.56	<19.50	AAA	<42.02	<28.51	<36.47	PPP	10.99	<0.27	<9.37
J10233658+4220477	718.84 ± 8.05	1085.12 ± 8.56	1265.47 ± 21.92	MMM	558.50 ± 21.07	239.08 ± 11.65	83.17 ± 9.48	PPP	10.81	9.52	10.05
J10233684+4221037	268.06 ± 8.05	346.87 ± 8.56	290.12 ± 21.92	MMM	195.67 ± 17.87	71.96 ± 12.90	<36.43	PPP	10.55	3.84	9.59
J10272950+0114490	746.29 ± 11.60	1175.20 ± 11.27	1262.90 ± 35.01	AAA	586.38 ± 47.10	251.36 ± 15.89	70.93 ± 9.21	PPP	10.42	1.91	9.44
J10325316+5306536	<17.50	47.03 ± 6.53	85.32 ± 18.46	AAA	<39.18	<36.44	<32.48	PPP	11.02	1.03	<9.46
J10332972+4404342	679.80 ± 7.60	1143.78 ± 13.46	1000.27 ± 23.74	AMM	561.42 ± 20.29	310.54 ± 13.69	113.35 ± 10.87	GPP	11.12	14.35	10.39
J10333162+4404212	211.61 ± 8.35	443.82 ± 13.46	779.93 ± 23.74	AMM	296.30 ± 31.67	119.29 ± 17.97	41.60 ± 9.00	GPP	10.93	4.17	9.99
J10364274+5447356	<15.18	<14.42	<15.42	AAA	<50.46	<41.84	<40.66	PPP	10.78	<0.17	<9.29
J10392338+3904501	<14.47	<16.22	54.88 ± 10.71	AAA	57.84 ± 10.40	23.99 ± 3.76	<32.84	PPP	10.72	<0.16	9.29
J10435053+0645466	908.74 ± 6.93	1426.00 ± 9.42	1527.20 ± 30.11	AAA	739.62 ± 55.76	268.30 ± 26.47	126.27 ± 13.54	APP	10.53	4.46	9.78
J10435268+0645256	70.02 ± 5.10	128.94 ± 5.83	345.66 ± 17.53	AAA	245.67 ± 22.10	116.31 ± 15.33	<76.56	APP	10.42	0.56	9.80
J10452478+3910298	112.42 ± 12.10	122.56 ± 7.02	244.20 ± 16.00	AAA	189.69 ± 18.59	81.94 ± 10.03	<40.28	APP	10.63	0.67	9.63
J10514450+5101303	<55.53	<53.29	<62.73	AAA	<35.27	<35.19	<32.71	PPP	10.80	<0.16	<8.66
J10595915+0857357	<14.47	<14.63	<20.26	AAA	<43.21	<28.80	<40.62	PPP	10.86	<0.32	<9.47

Table 2
(Continued)

(1) Galaxy ID (2MASX)	(2) F70 μm (mJy)	(3) F100 μm (mJy)	(4) F160 μm (mJy)	(5) P-PACS	(6) F250 μm (mJy)	(7) F350 μm (mJy)	(8) F500 μm (mJy)	(9) P-SPIRE	(10) $\log M_{\rm star}$ ($M_\odot$)	(11) SFR ($M_\odot$ yr^{-1})	(12) $\log M_{\rm gas}$ ($M_\odot$)
J11014364+5720336	<9.04	<178.93	<24.27	AAA	<58.01	<52.54	<64.05	PPP	10.54	<2.01	<9.37
J11064944+4751119	<11.86	<12.65	<13.89	AAA	<85.33	<48.39	<43.96	PPP	11.00	<0.30	<9.74
J11065068+4751090	259.74 ± 8.73	456.00 ± 9.30	519.09 ± 21.25	AAA	352.17 ± 24.81	134.43 ± 8.95	47.63 ± 10.59	PPP	11.11	8.47	10.22
J11204657+0028142	318.52 ± 38.33	275.79 ± 36.70	220.16 ± 12.98	AAA	87.88 ± 8.61	44.90 ± 8.95	<44.09	GPP	10.49	1.12	8.55
J11204801+0028068	<49.52	<47.52	<46.04	AAA	67.86 ± 9.51	<40.36	<46.21	GPP	10.80	<0.14	8.90
J11251704+0227007	<13.50	<17.16	<19.39	AAA	40.95 ± 10.25	<43.79	<51.00	PPP	10.72	<0.23	9.26
J11251716+0226488	51.04 ± 5.94	138.38 ± 9.60	219.03 ± 22.83	AAA	164.52 ± 12.36	87.73 ± 14.98	<45.87	PPP	10.97	1.13	9.96
J11273289+3604168	70.87 ± 5.20	154.65 ± 9.90	275.72 ± 13.37	AAA	185.12 ± 17.20	70.08 ± 9.25	46.05 ± 9.85	AGG	10.84	0.78	9.62
J11273467+3603470	624.34 ± 12.74	1417.00 ± 12.21	1887.00 ± 24.35	AAA	1180.76 ± 79.62	482.73 ± 14.53	158.63 ± 10.97	AGG	11.19	4.98	10.24
J11375801+4728143	<17.95	<19.32	<22.62	AAA	<76.98	<38.08	<51.27	PPP	10.75	<0.12	<9.20
J11440433+3332339	156.58 ± 6.84	334.38 ± 6.35	386.61 ± 11.86	AAA	277.05 ± 9.74	101.84 ± 20.70	<51.09	PPP	10.35	1.11	9.58
J11484370+3547002	245.71 ± 12.07	562.98 ± 11.80	928.88 ± 22.28	MMM	514.88 ± 37.78	216.07 ± 11.40	78.64 ± 10.56	PPP	10.94	7.84	10.44
J11484525+3547092	267.61 ± 12.07	598.32 ± 11.80	459.22 ± 22.28	MMM	402.27 ± 54.30	189.07 ± 11.91	53.54 ± 8.82	PPP	11.27	7.14	10.25
J11501333+3746107	<15.49	41.94 ± 3.82	124.04 ± 13.85	AAM	47.70 ± 7.24	<33.95	<33.85	PPP	10.84	0.66	9.40
J11501399+3746306	148.80 ± 5.95	320.16 ± 6.54	309.70 ± 13.85	AAM	248.53 ± 9.61	113.71 ± 7.55	44.04 ± 10.79	PPP	10.95	3.44	10.05
J11505764+1444200	<14.87	<14.06	<17.12	AAA	<25.48	<27.27	<26.19	PPP	10.87	<0.25	<9.19
J11542299+4932509	<14.52	<15.08	<16.62	AAA	35.45 ± 8.80	<32.56	<38.89	PPP	10.95	<0.42	9.49
J12020424+5342317	41.22 ± 5.33	71.54 ± 4.85	119.44 ± 10.72	AAA	97.15 ± 8.57	47.16 ± 6.46	<39.11	PPP	10.88	1.78	10.03
J12054066+0135365	<34.41	<42.56	<32.47	AAA	<43.02	<36.57	<39.41	AAA	10.21	<0.09	<8.61
J12115507+4039182	467.63 ± 21.33	690.98 ± 20.83	851.82 ± 43.60	MMM	264.79 ± 20.04	123.73 ± 15.98	<67.02	PPP	10.40	1.08	9.14
J12115648+4039184	2413.87 ± 21.33	2090.60 ± 20.83	1031.37 ± 43.60	MMM	467.84 ± 17.31	155.57 ± 10.70	90.97 ± 11.70	PPP	10.36	7.14	9.12
J12191866+1201054	164.66 ± 7.39	237.80 ± 7.52	392.89 ± 26.58	AAA	189.20 ± 11.91	82.43 ± 14.21	35.33 ± 8.12	PPP	10.12	0.83	9.34
J12433887+4405399	93.44 ± 6.88	190.87 ± 7.06	291.07 ± 16.53	AAA	189.84 ± 11.52	82.28 ± 12.26	<29.52	PPP	10.84	1.17	9.64
J12525011+4645272	51.06 ± 5.86	106.38 ± 5.43	124.40 ± 4.74	AAA	122.60 ± 9.68	58.86 ± 10.75	<44.78	PPP	11.05	1.84	10.07
J13011662+4803366	922.45 ± 11.95	1206.16 ± 12.70	1144.11 ± 30.74	MMM	504.63 ± 36.55	198.88 ± 11.70	74.39 ± 10.65	PPP	10.51	5.62	9.62
J13011835+4803304	675.05 ± 11.95	975.24 ± 12.70	845.78 ± 30.74	MMM	366.05 ± 31.51	162.10 ± 11.22	47.29 ± 11.94	PPP	10.31	2.94	9.43
J13082737+0422125	54.10 ± 7.99	124.30 ± 6.83	179.01 ± 14.30	AAA	139.97 ± 14.04	75.34 ± 7.13	33.20 ± 5.76	GPP	9.84	0.28	9.35
J13082964+0422045	74.68 ± 7.92	149.92 ± 8.14	222.27 ± 12.76	AAA	171.76 ± 10.19	93.85 ± 14.69	35.38 ± 6.46	GPP	10.22	0.38	9.43
J13131470+3910382	<23.14	<24.15	<67.02	AAA	<33.20	<36.51	<31.20	PPP	10.92	<0.68	<9.48
J13151386+4424264	256.70 ± 11.79	483.17 ± 6.95	569.02 ± 13.79	AAA	411.36 ± 35.87	164.61 ± 16.70	<80.63	APP	10.73	2.35	9.88
J13151726+4424255	1105.10 ± 9.30	1094.20 ± 8.30	669.71 ± 20.69	AAA	340.75 ± 31.14	138.57 ± 11.12	<61.67	APP	11.04	8.29	9.41
J13153076+6207447	1894.62 ± 24.13	2488.20 ± 21.36	2602.03 ± 63.41	MMM	923.01 ± 78.71	320.41 ± 44.00	116.71 ± 26.82	APP	10.62	7.59	9.80
J13153506+6207287	9522.37 ± 24.13	8581.77 ± 21.36	5586.27 ± 63.41	MMM	1615.77 ± 135.74	539.46 ± 41.27	167.12 ± 24.28	APP	10.80	55.30	9.81
J13325525–0301347	423.10 ± 11.84	542.11 ± 12.36	416.85 ± 20.37	MMM	300.33 ± 12.92	93.49 ± 10.37	<33.69	PPP	10.62	7.08	9.67
J13325655–0301395	276.81 ± 11.84	476.79 ± 12.36	612.95 ± 20.37	MMM	281.72 ± 19.14	148.02 ± 12.66	49.38 ± 9.48	PPP	10.91	4.37	9.91
J13462001–0325407	34.85 ± 4.92	202.52 ± 10.65	309.66 ± 25.46	AAA	223.82 ± 18.24	107.98 ± 12.36	42.40 ± 7.74	AAP	10.69	0.28	9.45
J14003661–0254327	<41.24	25.07 ± 4.92	<51.99	AAA	<32.23	<24.77	<42.83	PPP	10.60	0.08	<8.63
J14003796–0254227	<13.46	<16.89	<15.99	AAA	<48.94	<29.11	<30.13	PPP	10.55	<0.06	<8.82
J14005783+4251203	1101.70 ± 9.93	1573.70 ± 11.16	1726.93 ± 39.41	AAM	893.18 ± 69.75	352.67 ± 29.30	129.50 ± 12.79	APP	10.71	8.10	10.01
J14005879+4250427	1407.30 ± 10.47	1788.80 ± 12.41	1798.37 ± 39.41	AAM	849.70 ± 62.63	303.06 ± 19.83	99.48 ± 14.24	APP	10.60	9.88	9.86
J14055079+6542598	81.29 ± 6.76	161.01 ± 6.26	221.49 ± 10.95	AAA	182.80 ± 17.26	103.07 ± 10.63	55.79 ± 9.48	APP	10.30	0.73	9.80
J14062157+5043303	4848.30 ± 25.34	8820.20 ± 24.14	10480.00 ± 58.91	AAA	4350.49 ± 166.18	1990.01 ± 76.04	695.15 ± 63.28	AAA	10.14	0.92	9.32
J14070703–0234513	44.43 ± 5.16	165.84 ± 9.56	220.38 ± 10.74	AAA	164.48 ± 15.13	86.58 ± 8.92	36.21 ± 8.79	PPP	10.98	1.49	10.01
J14234238+3400324	954.06 ± 8.13	1465.10 ± 12.39	1596.00 ± 22.30	AAA	789.00 ± 58.13	360.55 ± 28.53	124.10 ± 13.66	AAP	10.06	0.97	9.23
J14234632+3401012	237.13 ± 8.52	499.65 ± 11.25	698.09 ± 17.35	AAA	446.27 ± 42.09	224.34 ± 22.98	76.06 ± 11.45	AAP	10.16	0.26	9.08
J14245831–0303597	253.64 ± 7.85	591.09 ± 11.13	857.00 ± 22.18	AAA	325.65 ± 16.98	115.16 ± 15.83	<53.15	GPP	10.91	4.07	9.96

Table 2
(Continued)

(1) Galaxy ID (2MASX)	(2) F70 μm (mJy)	(3) F100 μm (mJy)	(4) F160 μm (mJy)	(5) P-PACS	(6) F250 μm (mJy)	(7) F350 μm (mJy)	(8) F500 μm (mJy)	(9) P-SPIRE	(10) log $M_{\rm star}$ ($M_\odot$)	(11) SFR ($M_\odot$ yr^{-1})	(12) log $M_{\rm gas}$ ($M_\odot$)
J14245913–0304012	<40.60	<43.69	<27.89	AAA	222.15 ± 16.49	129.20 ± 15.86	61.39 ± 13.81	GPP	11.12	<0.62	9.92
J14250739+0313560	<15.68	<13.71	<13.43	AAA	<39.41	<33.13	<33.58	PPP	10.36	<0.10	<9.01
J14294766+3534275	18.04 ± 3.67	<175.35	49.51 ± 12.07	AAA	66.45 ± 10.80	<65.79	<46.34	APP	10.97	<0.68	9.02
J14295031+3534122	180.58 ± 5.65	283.04 ± 15.59	254.06 ± 9.01	AAA	177.90 ± 16.70	61.32 ± 9.05	<49.03	APP	10.60	1.06	9.24
J14334683+4004512	886.49 ± 12.00	1345.40 ± 14.96	1763.50 ± 37.31	AAM	892.53 ± 74.85	446.44 ± 41.59	206.70 ± 10.84	AAG	10.94	4.38	10.11
J14334840+4005392	1459.00 ± 12.23	2146.80 ± 10.61	2496.30 ± 37.31	AAM	1102.57 ± 85.57	462.39 ± 36.70	136.34 ± 8.90	AAG	10.79	5.30	9.81
J14442055+1207429	258.73 ± 11.30	392.32 ± 12.00	565.22 ± 29.96	MMM	180.05 ± 20.87	164.41 ± 12.67	68.79 ± 11.10	GGP	10.76	1.15	9.21
J14442079+1207552	574.60 ± 11.30	1234.18 ± 12.00	1598.18 ± 29.96	MMM	895.89 ± 22.73	287.70 ± 10.92	117.72 ± 10.60	GGP	11.11	3.48	10.05
J15002500+4317131	27.94 ± 5.11	<18.18	16.77	AAA	<45.82	<52.13	<48.99	PPP	10.73	<0.10	<8.96
J15053137+3427534	<13.13	<14.13	<12.73	AAA	<35.21	<36.48	<34.79	PPP	11.00	<0.44	<9.53
J15064391+0346364	33.08 ± 7.23	32.59 ± 7.23	<85.47	AAA	<45.73	<42.30	<35.47	GGP	10.93	0.21	<9.04
J15064579+0346214	232.45 ± 9.24	477.59 ± 13.24	780.68 ± 66.13	AAA	441.27 ± 36.88	202.46 ± 10.04	88.87 ± 10.08	GGP	10.86	2.22	9.97
J15101587+5810425	41.02 ± 10.00	<18.51	<24.37	MMM	<66.01	<39.97	<37.62	PPP	10.70	<0.09	<9.07
J15101776+5810375	304.72 ± 10.00	697.73 ± 9.03	806.48 ± 65.40	MMM	427.43 ± 21.74	176.68 ± 7.71	62.51 ± 10.13	PPP	10.50	2.04	9.68
J15144544+0403587	<26.81	39.84 ± 7.79	<69.46	AAA	64.47 ± 12.30	29.82 ± 7.12	<35.19	PPP	10.83	0.29	9.21
J15144697+0403576	<17.54	<18.90	<48.40	AAA	<33.51	<30.61	<35.12	PPP	10.77	<0.15	<8.99
J15233768+3749030	130.26 ± 6.35	164.97 ± 5.60	154.33 ± 17.71	AAA	119.51 ± 12.49	47.45 ± 8.17	<53.55	APP	10.14	0.47	8.95
J15264774+5915464	<14.01	<12.35	<15.42	AAA	<28.48	<23.89	<29.13	PPP	10.77	<0.14	<9.06
J15281276+4255474	1502.20 ± 17.05	3183.20 ± 20.78	3633.40 ± 41.97	AAA	1966.20 ± 114.11	807.69 ± 54.68	294.20 ± 29.05	AAA	10.96	2.93	9.91
J15281667+4256384	84.09 ± 6.07	147.59 ± 5.43	192.57 ± 21.48	AAA	72.08 ± 10.49	<58.76	<49.29	AAA	10.70	0.14	8.46
J15523393+4620237	110.88 ± 6.21	261.34 ± 7.68	385.20 ± 20.21	AAA	267.30 ± 14.16	116.31 ± 8.99	38.57 ± 7.70	PPP	10.92	3.53	10.16
J15562191+4757172	522.75 ± 7.89	721.78 ± 7.39	761.40 ± 17.63	AAA	466.39 ± 34.08	198.57 ± 19.07	66.37 ± 7.78	AAP	10.15	1.50	9.37
J15583749+3227379	<8.29	<8.79	<10.26	AAA	78.57 ± 18.18	32.05 ± 7.55	<25.68	PPP	10.56	<0.12	9.50
J15583784+3227471	349.87 ± 6.76	627.04 ± 7.22	702.98 ± 12.78	AAA	361.72 ± 20.96	151.29 ± 5.88	41.59 ± 7.21	PPP	10.89	4.81	9.89
J16024254+4111499	1442.55 ± 14.88	2267.31 ± 12.52	2364.66 ± 28.23	MMM	1056.54 ± 27.49	470.49 ± 34.98	184.42 ± 11.57	GPP	10.81	10.66	10.13
J16024475+4111589	413.45 ± 14.88	691.29 ± 12.52	910.24 ± 28.23	MMM	380.22 ± 16.91	182.97 ± 18.21	67.52 ± 9.14	GPP	10.48	2.84	9.71
J16080559+2529091	<92.56	214.78 ± 9.41	558.62 ± 20.08	MMM	181.27 ± 14.99	<67.98	<58.70	PPP	10.90	1.78	9.67
J16080648+2529066	131.04 ± 14.51	240.68 ± 9.41	122.49 ± 20.08	MMM	342.93 ± 19.66	198.37 ± 18.06	<56.18	PPP	11.16	2.14	10.08
J16082261+2328459	138.82 ± 9.96	267.16 ± 8.47	669.17 ± 33.34	AAM	326.25 ± 13.67	99.03 ± 12.32	57.11 ± 8.58	GPP	10.38	1.82	9.93
J16082354+2328240	951.20 ± 6.74	1278.60 ± 16.78	1109.63 ± 33.34	AAM	488.88 ± 18.52	263.92 ± 11.27	72.67 ± 7.70	GPP	10.67	10.37	9.95
J16145418+3711064	<22.82	24.92 ± 4.90	<22.74	AAA	<30.49	<46.44	<47.06	PPP	11.12	0.46	<9.29
J16282497+4110064	<51.50	<52.55	<45.85	AAA	<38.44	<40.42	<37.49	APP	10.89	<0.29	<8.93
J16282756+4109395	18.13 ± 3.50	57.43 ± 5.41	40.50 ± 9.25	AAA	<38.44	<31.81	<37.19	APP	10.83	0.30	<8.90
J16354293+2630494	25.36 ± 5.11	33.53 ± 5.36	59.02 ± 12.87	AAA	<38.60	<41.14	<36.54	PPP	11.23	0.90	<9.52
J16372583+4650161	41.58 ± 6.93	107.55 ± 6.02	308.13 ± 24.89	AAM	140.86 ± 9.72	106.33 ± 18.11	53.50 ± 9.39	GPP	11.26	1.64	10.20
J16372754+4650054	69.34 ± 7.52	179.90 ± 8.12	205.43 ± 24.89	AAM	267.81 ± 7.56	<109.99	<59.72	GPP	10.98	2.09	10.19
J17020378+1859495	<20.26	<18.22	<23.73	AAA	<28.63	<37.35	<31.44	PPP	10.67	<0.31	<9.23
J17045089+3448530	303.07 ± 8.38	479.89 ± 9.62	156.54 ± 30.62	MMM	300.39 ± 34.50	<117.59	<66.97	PPP	10.74	7.42	9.88
J17045097+3449020	1310.33 ± 8.38	1628.11 ± 9.62	1808.06 ± 30.62	MMM	654.28 ± 36.22	298.36 ± 29.33	88.79 ± 16.17	PPP	10.99	24.71	10.21
J20471908+0019150	1002.60 ± 63.17	1419.10 ± 54.45	3087.20 ± 74.43	AAA	2383.84 ± 105.02	1214.49 ± 76.78	481.05 ± 32.56	AAA	11.09	1.83	10.18

Note. Descriptions of columns: (1) Galaxy ID, taken from 2MASS. (2) *Herschel* PACS 70 μm flux (mJy). (3) *Herschel* PACS 100 μm flux (mJy). (4) *Herschel* PACS 160 μm flux (mJy). (5) *Herschel* PACS photometric methods, "A": aperture, "M": model fitting, "C": compact. (6) *Herschel* SPIRE 250 μm flux (mJy). (7) *Herschel* SPIRE 350 μm flux (mJy). (8) *Herschel* SPIRE 500 μm flux (mJy). (9) *Herschel* SPIRE photometric methods, "A": aperture, "P": PSF fitting, "G": Gaussian fitting. (10) Stellar mass (log($M_\odot$)). (11) Star formation rate ($M_\odot$ yr^{-1}). (12) Total gas mass (log($M_\odot$)).

(This table is available in machine-readable form.)

Table 3
Herschel 6-band Fluxes and Physical Parameters of H-KPAIR Ellipticals

(1) Galaxy ID (2MASX)	(2) F70 μm (mJy)	(3) F100 μm (mJy)	(4) F160 μm (mJy)	(5) P-PACS	(6) F250 μm (mJy)	(7) F350 μm (mJy)	(8) F500 μm (mJy)	(9) P-SPIRE	(10) log $M_{\rm star}$ ($M_\odot$)	(11) SFR ($M_\odot$ yr^{-1})	(12) log $M_{\rm gas}$ ($M_\odot$)
J00202748+0050009	<25.37	32.41 ± 7.31	91.59 ± 12.06	AAA	55.55 ± 10.24	<48.28	<46.92	APP	10.75	0.06	8.62
J03381299+0109414	326.73 ± 12.60	647.89 ± 9.68	837.69 ± 22.90	AAA	<32.20	<67.56	<62.95	APP	10.55	4.85	<9.03
J08083563+3854522	<18.58	<16.62	<18.30	AAA	<29.87	<37.62	<51.16	PPP	10.89	<0.15	<8.99
J08385973+3613164	<59.26	31.69 ± 5.30	<29.82	AAA	<41.85	<47.14	<37.81	PPP	11.12	0.53	<9.37
J08415054+2642475	<12.21	<14.45	<12.85	AAA	<34.25	<20.46	<29.21	PPP	11.13	<0.62	<9.64
J09060283+5144411	<20.84	<21.48	<21.92	AAA	<33.19	<24.55	<51.83	AAP	10.70	<0.10	<8.80
J09123636+3547180	<20.22	<18.51	<21.32	AAA	<31.78	<45.99	<44.77	PPP	10.56	<0.06	<8.61
J09134461+4742165	<10.53	17.28 ± 3.35	<25.01	AAA	64.80 ± 11.55	44.85 ± 8.38	<32.64	GGP	11.10	0.25	9.46
J09374506+0244504	<49.45	<57.59	<65.53	AAA	129.50 ± 15.27	107.02 ± 16.36	80.00 ± 15.11	AAA	10.96	<0.15	9.09
J10155338+0657495	25.62 ± 4.03	33.36 ± 4.06	26.67 ± 5.34	AAA	<61.30	<50.34	<57.53	PPP	10.81	0.14	<8.98
J10205369+4831246	<18.30	20.07 ± 3.82	48.91 ± 6.01	AAA	46.45 ± 10.62	<33.10	<36.51	PPP	10.99	0.31	9.37
J10272970+0115170	<46.39	<45.08	<58.29	AAA	<76.12	<42.78	<49.04	PPP	10.76	<0.12	<8.88
J10325321+5306477	<17.50	<16.11	<20.65	AAA	50.93 ± 10.39	<35.66	<36.89	PPP	11.20	<0.37	9.55
J10364400+5447489	<15.18	27.10 ± 4.76	57.72 ± 11.39	AAA	<30.85	<23.60	<41.35	PPP	11.12	0.31	<9.11
J10392515+3904573	<14.47	<16.22	<21.51	AAA	<38.05	<21.70	<33.19	PPP	10.79	<0.16	<9.13
J10452496+3909499	<28.51	<38.90	<34.46	AAA	<35.64	<36.29	<31.78	APP	10.68	<0.13	<8.71
J10514368+5101195	47.68 ± 6.11	99.25 ± 6.01	138.40 ± 17.17	AAA	55.87 ± 10.04	<33.47	<29.42	PPP	11.12	0.18	8.71
J10595869+0857215	<14.47	<14.63	<20.26	AAA	<47.95	<27.39	<44.41	PPP	11.23	<0.32	<9.50
J11014357+5720058	<9.04	<178.93	<24.27	AAA	<55.69	<66.14	<85.02	PPP	10.80	<1.93	<9.34
J11375476+4727588	<24.93	<26.84	<72.58	AAA	<37.68	<30.10	<45.17	PPP	10.99	<0.17	<8.95
J11440335+3332062	89.03 ± 6.78	192.15 ± 7.59	193.80 ± 8.79	AAA	105.13 ± 11.00	<62.13	<34.15	PPP	10.73	0.48	9.04
J11505844+1444124	<20.46	<19.35	<22.64	AAA	<25.34	<28.65	<33.72	PPP	11.24	<0.32	<9.18
J11542307+4932456	<14.52	<15.08	<16.62	AAA	<33.47	<33.82	<32.59	PPP	11.35	<0.43	<9.48
J12020537+5342487	<14.04	<12.79	<13.48	AAA	<34.01	<33.20	<43.16	PPP	11.09	<0.30	<9.40
J12054073+0134302	<16.63	<20.56	<17.76	AAA	<43.02	<36.57	<39.41	AAA	10.52	<0.04	<8.57
J12191719+1200582	<24.65	<25.10	<33.60	AAA	<35.82	<39.65	<28.11	PPP	10.53	<0.09	<8.73
J12433936+4406046	<14.76	<15.11	<16.20	AAA	<46.90	<38.94	<27.56	PPP	10.88	<0.14	<9.16
J12525212+4645294	47.54 ± 4.72	59.27 ± 5.71	80.75 ± 8.80	AAA	47.91 ± 10.15	<29.37	<50.12	PPP	11.14	1.47	9.47
J13131429+3910360	<23.14	<24.15	<67.02	AAA	<24.10	<33.87	<28.42	PPP	11.26	<0.68	<9.36
J13462215–0325057	30.10 ± 4.24	54.45 ± 5.69	65.60 ± 7.45	AAA	<37.54	<27.94	<27.52	AAP	10.53	0.16	<8.68
J14055334+6542277	26.07 ± 4.78	<20.03	<31.41	AAA	<46.59	<26.44	<37.84	APP	10.62	<0.10	<8.96
J14064127+5043239	<204.35	<138.04	<124.38	AAA	<45.17	<51.68	<70.05	AAA	10.30	<0.04	<7.85
J14070720–0234402	<22.89	<24.17	<20.88	AAA	<53.97	<36.13	<35.11	PPP	10.76	<0.41	<9.46
J14250552+0313590	59.56 ± 6.02	101.37 ± 7.03	97.44 ± 14.59	AAA	61.35 ± 9.52	37.92 ± 7.03	<35.97	PPP	10.75	0.58	9.14
J15002374+4316559	37.39 ± 7.52	19.76 ± 3.59	<23.67	AAA	<32.89	<36.62	<45.18	PPP	10.88	0.10	<8.82
J15053183+3427526	<13.13	<14.13	<12.73	AAA	<34.70	<33.02	<31.14	PPP	11.24	<0.43	<9.52
J15233899+3748254	<20.50	<18.09	<24.72	AAA	38.32 ± 9.46	<36.84	<38.41	APP	10.19	<0.05	8.67
J15264892+5915478	<14.01	<12.35	<15.42	AAA	<25.85	<25.94	<28.87	PPP	10.91	<0.14	<9.04
J15523258+4620180	<15.23	<14.07	<17.84	AAA	<35.36	<40.27	<32.18	PPP	11.17	<0.28	<9.36
J15562738+4757302	<16.61	<15.53	<16.63	AAA	<40.91	<47.06	<39.00	AAP	10.17	<0.03	<8.58
J16145421+3711136	<22.82	<19.59	<22.74	AAA	<31.27	<43.27	<50.60	PPP	11.16	<0.36	<9.30
J16354366+2630505	<14.64	<15.37	<16.04	AAA	<40.94	<40.90	<41.63	PPP	11.27	<0.44	<9.55
J17020320+1900006	<20.26	<18.22	55.42 ± 13.02	AAA	<28.45	<38.78	<31.68	PPP	11.00	<0.33	<9.25
J20472428+0018030	<61.19	<54.39	<61.46	AAA	<48.59	<51.33	<52.71	AAA	10.74	<0.05	<8.30

Note. Descriptions of Columns: (1) Galaxy ID, taken from 2MASS. (2) *Herschel* PACS 70 μm flux (mJy). (3) *Herschel* PACS 100 μm flux (mJy). (4) *Herschel* PACS 160 μm flux (mJy). (5) *Herschel* PACS photometric methods, "A": aperture, "M": model fitting, "C": compact. (6) *Herschel* SPIRE 250 μm flux (mJy). (7) *Herschel* SPIRE 350 μm flux (mJy). (8) *Herschel* SPIRE 500 μm flux (mJy). (9) *Herschel* SPIRE photometric methods, "A": aperture, "P": PSF fitting, "G": Gaussian fitting. (10) Stellar mass (log($M_\odot$)). (11) Star formation rate ($M_\odot$ yr^{-1}). (12) Total gas mass (log($M_\odot$)).

(This table is available in machine-readable form.)

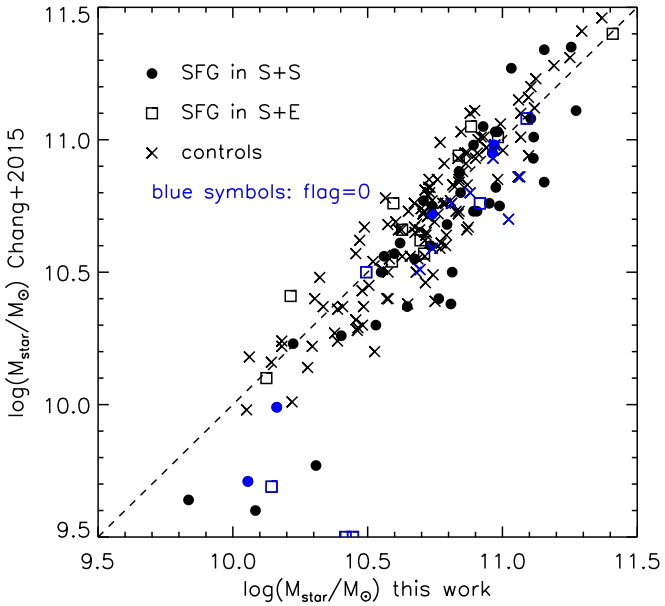

Figure 5. Comparison of stellar masses estimated in our work and in Chang et al. (2015). Star-forming spirals in S+S pairs are shown as black dots, those in S+E pairs are shown as open squares, and SFGs in the control sample are shown as crosses.

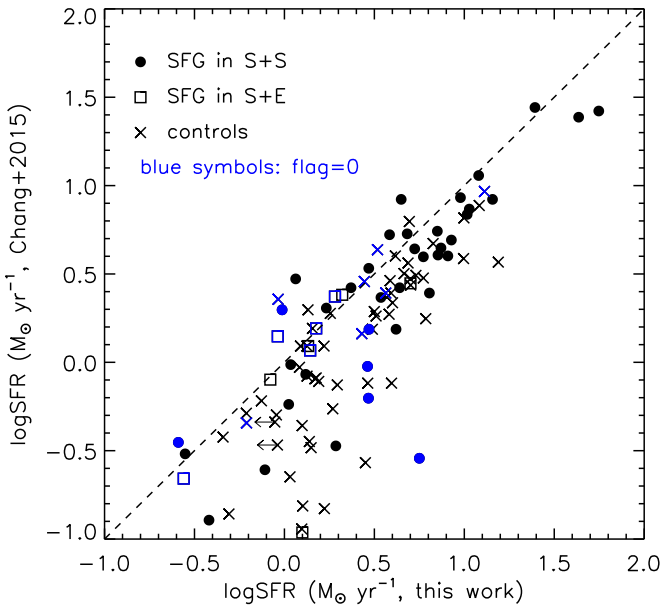

Figure 6. Comparison of SFRs estimated in our work and in Chang et al. (2015). Star-forming spirals in S+S pairs are shown as black dots, those in S+E pairs are shown as open squares, and SFGs in the control sample are shown as crosses.

upper limits are well mixed (Feigelson & Nelson 1985). In order to confirm that this is indeed the case, the following test was carried out: a hybrid sample was constructed by replacing those galaxies in the control sample that matched to the low sSFR H-KPAIR galaxies ($\log(\mathrm{sSFR/yr^{-1}})$ values/upper limits below -11.3) with the H-KPAIR galaxies themselves. Again using the K–M estimator, we found a mean $\log(\mathrm{sSFR/yr^{-1}}) = -10.94 \pm 0.05$ for such a sample, significantly lower than the result for the control sample. The implicit assumption in this test is that below $\log(\mathrm{sSFR/yr^{-1}}) = -11.3$ the control and H-KPAIR samples have nearly identical sSFR distributions, which is reasonable if the red spirals with low sSFRs are similar to early-type galaxies that show no interaction-induced star formation enhancement (Sulentic 1989).

In Figure 7 we plotted the lines representing the blue sequence and the red sequence, taken from Figure 7 of Schiminovich et al. (2007), where it is also shown that galaxies with $\log(\mathrm{sSFR/yr^{-1}}) < -11.3$ belong to the red sequence.

In order to minimize the bias due to the mismatch, we confined the star formation enhancement analysis to H-KPAIR galaxies with values/upper limits of $\log(\mathrm{sSFR/yr^{-1}}) \geqslant -11.3$ and the control galaxies matched to them. Among these 101 paired SFG galaxies, the sSFR of 5 galaxies are upper limits; for their matches in the control sample, 19 have the sSFR in upper limits. It is possible that the true values of some of the upper limits are below the $\log(\mathrm{sSFR})$ cutoff. However, they are only small fractions of both samples. Furthermore, because in the K–S estimator the probability distributions of the true values of the upper limits are estimated using data points included in the analysis (none of them is below the cutoff), the possible contamination by low sSFR red spirals should not significantly affect the mean sSFR of SFGs in both the H-KPAIR and control samples.

We found a mean of $\log(\mathrm{sSFR/yr^{-1}}) = -10.34 \pm 0.05$ for SFGs in the H-KPAIR, and $\log(\mathrm{sSFR/yr^{-1}}) = -10.67 \pm 0.04$ for their matches in the control sample. The corresponding sSFR enhancement (Xu et al. 2010) is $\mathrm{enh} = \langle\log(\mathrm{sSFR})\rangle_{\mathrm{pair}} - \langle\log(\mathrm{sSFR})\rangle_{\mathrm{cont}} = 0.33 \pm 0.06$. This indicates that the sSFR of paired SFGs is enhanced on average by a factor of $\sim$2 compared to control galaxies, and the enhancement is significant at the $>5\sigma$ level. When paired SFGs are divided into subsamples of galaxies in S+S pairs and in S+E pairs, we found a mean of $\log(\mathrm{sSFR/yr^{-1}}) = -10.21 \pm 0.06$ for the S+S subsample and $\log(\mathrm{sSFR/yr^{-1}}) = -10.64 \pm 0.07$ for the S+E subsample. This shows that SFGs in S+S pairs have strong sSFR enhancement (with $\mathrm{enh} = 0.46 \pm 0.08$) and those in S+E have no significant sSFR enhancement. The result is in very good agreement with that of (Xu et al. 2010) based on *Spitzer* observations of a smaller subsample of KPAIR. We further divided the S+S and S+E subsamples by the interaction morphology (INT/MER vs JUS), and found that the mean values for SFGs in S+S pairs of INT/MER types and of JUS type are $\log(\mathrm{sSFR/yr^{-1}}) = -10.14 \pm 0.07$ and $\log(\mathrm{sSFR/yr^{-1}}) = -10.31 \pm 0.08$, respectively. This suggests that SFGs in S+S pairs of INT and MER types are slightly more enhanced (by 0.17 dex) than those in JUS pairs, though the significance of the difference is only at the 1.5σ level. No significant sSFR enhancement is found for SFGs in S+E pairs of either the INT/MER types (mean $\log(\mathrm{sSFR/yr^{-1}}) = -10.58 \pm 0.11$) or the JUS type (mean $\log(\mathrm{sSFR/yr^{-1}}) = -10.71 \pm 0.11$).

In Figure 8 we compared the sSFR of SFGs in S+S pairs and S+E pairs with the controls in four M_{star} bins ($\log(M_{\mathrm{star}}/M_{\odot}) < 10.4$, $10.4 \leqslant \log(M_{\mathrm{star}}/M_{\odot}) < 10.7$, and $10.7 \leqslant \log(M_{\mathrm{star}}/M_{\odot})$). For SFGs in S+S pairs we found a similar amount of sSFR enhancement in different M_{dust} bins. For SFGs in S+E pairs no significant sSFR enhancement is found in any M_{dust} bin. It is worth noting that Xu et al. (2010) found that SFGs in S+S pairs in their lowest M_{star} bin (corresponding to $9.3 < \log(M_{\mathrm{star}}/M_{\odot}) < 9.8$ for the M_{star} calibration used in this paper) do not show any significant sSFR enhancement. These low-mass galaxies are not included in H-KPAIR because of the exclusion of pairs of $v < 2000$ km s^{-1}.

Table 4
Herschel 5-band Fluxes and Physical Parameters of Spirals in the Control Sample

(1) Galaxy ID (Control)	(2) R.A. (J2000)	(3) decl. (J2000)	(4) z redshift	(5) F100 μm (mJy)	(6) F160 μm (mJy)	(7) F250 μm (mJy)	(8) F350 μm (mJy)	(9) F500 μm (mJy)	(10) log $M_{\rm star}$ (log $M_{\odot}$)	(11) SFR ($M_{\odot}$ yr^{-1})	(12) log $M_{\rm gas}$ (log $M_{\odot}$)	(13) Galaxy ID (Pair)
lk-096	164.74153	58.133747	0.0319167	146.43 ± 7.43	253.13 ± 9.49	168.30 ± 11.17	90.81 ± 15.02	<65.03	10.58	0.49	9.61	J00202580+0049350
lk-416	158.55316	57.079830	0.0482240	113.78 ± 6.87	244.52 ± 10.39	212.03 ± 16.14	107.13 ± 22.57	<104.06	10.88	1.17	10.20	J01183417–0013416
lk-075	158.30994	56.741673	0.0468842	<43.80	<53.66	<107.36	<100.03	<135.08	10.71	<0.50	<9.57	J01183556–0013594
egs-009	213.96425	51.856659	0.0456582	171.32 ± 6.56	291.75 ± 7.25	156.07 ± 12.94	79.33 ± 13.09	<49.66	10.46	1.23	9.76	J02110638–0039191
en1-045	242.20769	53.997375	0.0627264	34.02 ± 7.18	56.46 ± 8.34	60.07 ± 10.28	<67.36	<58.72	10.58	0.72	9.59	J02110832–0039171
lk-244	161.47475	56.506535	0.0461360	83.70 ± 8.18	161.28 ± 8.62	112.31 ± 9.62	49.64 ± 12.35	<54.88	10.73	0.90	9.58	J03381222+0110088
lk-108	159.86114	57.662411	0.0719180	<26.53	<36.79	<43.59	<86.05	<52.88	10.86	<0.76	<9.59	J07543194+1648214
lk-368	163.04863	58.438011	0.0315815	1061.65 ± 14.82	1822.36 ± 13.97	1049.99 ± 13.65	500.07 ± 9.39	194.86 ± 12.86	11.06	3.29	10.28	J07543221+1648349
en1-016	242.03619	53.878147	0.0641164	135.56 ± 6.36	238.76 ± 7.81	118.15 ± 12.24	60.87 ± 12.12	<90.64	10.69	1.80	9.92	J08083377+3854534
lk-290	165.13409	57.497932	0.0275216	<26.97	<41.11	<53.30	<41.20	<84.54	10.18	<0.11	<8.91	J08233266+2120171
lk-148	164.15407	59.215527	0.0325229	40.95 ± 7.85	114.71 ± 12.27	<60.81	66.83 ± 11.68	<64.11	10.38	0.22	<9.09	J08233421+2120515
lk-390	160.60169	58.458820	0.0451383	<25.89	65.22 ± 8.39	<36.63	<55.28	<57.79	10.65	<0.28	<9.16	J08291491+5531227
lk-248	162.23958	56.620098	0.0468625	79.00 ± 7.22	175.56 ± 11.18	163.64 ± 13.32	102.59 ± 14.25	<66.15	10.71	1.01	10.26	J08292083+5531081
lk-282	164.20754	57.412735	0.0468024	37.15 ± 7.00	<38.31	<61.42	<73.00	<51.33	10.91	0.43	<9.37	J08364482+4722188
lk-171	163.19229	60.094456	0.0697656	289.83 ± 7.96	463.92 ± 11.13	279.43 ± 28.53	97.37 ± 20.75	<126.28	11.06	4.95	10.24	J08364588+4722100
lk-405	159.23137	58.560928	0.0715059	<31.49	78.56 ± 8.87	<54.77	<63.28	<55.17	10.71	<0.88	<9.66	J08381759+3054534
lk-271	161.58758	56.765396	0.0672263	142.12 ± 7.21	177.08 ± 8.76	145.22 ± 9.67	89.74 ± 9.71	<53.52	10.94	3.52	10.32	J08381795+3055011
lk-009	163.78018	59.654129	0.0451426	858.23 ± 13.86	948.72 ± 17.93	531.34 ± 30.12	185.74 ± 36.85	<156.50	10.81	5.39	10.03	J08390125+3613042
btsh-212	218.07066	33.590675	0.0847390	101.22 ± 7.29	280.92 ± 8.35	214.35 ± 12.92	112.67 ± 12.23	<54.57	11.46	3.22	10.65	J08414959+2642578
lk-327	158.39201	57.133083	0.0466682	123.93 ± 7.39	260.04 ± 9.79	143.05 ± 21.06	<112.46	<120.05	10.66	1.34	9.67	J09060498+5144071
btsh-111	218.37558	34.561275	0.0287766	133.23 ± 6.08	179.24 ± 9.26	139.30 ± 8.88	<65.03	<60.62	10.34	0.54	9.29	J09123676+3547462
egs-043	214.41007	52.693192	0.0631147	<24.61	34.02 ± 7.12	<39.34	<47.90	<56.15	10.97	<0.54	<9.45	J09134606+4742001
lk-276	162.26814	56.911495	0.0718246	<25.25	<35.21	57.55 ± 13.64	88.90 ± 11.89	83.98 ± 16.52	10.73	<0.72	9.69	J09155467+4419510
btsh-146	218.82675	35.118813	0.0284341	5395.36 ± 35.44	5274.42 ± 52.53	1902.35 ± 32.67	725.94 ± 33.25	254.42 ± 24.96	11.02	12.96	10.05	J09155552+4419580
lk-056	161.98213	57.188320	0.0898139	<26.02	<45.15	<42.39	<48.52	<58.04	11.00	<1.20	<9.76	J09264111+0447247
lk-175	158.62358	59.784828	0.0905889	122.43 ± 15.91	109.51 ± 23.54	153.42 ± 24.42	111.23 ± 23.32	<138.69	11.37	5.27	10.78	J09264137+0447260
en1-018	242.25880	53.743439	0.0643115	43.30 ± 7.09	44.96 ± 9.26	<76.72	<54.51	<73.00	11.12	0.96	<9.70	J09374413+0245394
en1-048	242.60513	53.779949	0.0658474	148.85 ± 6.95	251.71 ± 9.55	197.29 ± 17.72	107.12 ± 16.14	<58.32	10.79	3.87	10.42	J10100079+5440198
lk-150	164.46387	59.365425	0.0461592	786.03 ± 11.98	863.67 ± 21.83	423.96 ± 19.93	200.22 ± 21.31	<103.25	10.77	6.11	10.01	J10100212+5440279
lk-256	162.47282	56.647766	0.0459531	103.97 ± 6.84	181.74 ± 10.33	112.72 ± 9.52	51.06 ± 10.78	<59.50	10.48	0.75	9.64	J10155257+0657330
btsh-148	218.99033	35.172455	0.0540843	74.98 ± 11.19	120.83 ± 11.79	85.83 ± 11.99	<61.30	<53.69	10.52	1.12	9.60	J10205188+4831096
lk-323	158.20479	56.945797	0.0569093	<54.04	122.49 ± 15.06	<105.94	<122.96	<111.23	10.61	<0.91	<9.72	J10225647+3446564
lk-155	158.16884	58.766632	0.0735668	<28.58	<40.19	<57.93	<62.76	<55.66	10.93	<0.86	<9.71	J10225655+3446468
lk-014	161.36885	59.496750	0.0724664	42.32 ± 7.49	97.26 ± 9.76	75.35 ± 8.81	54.89 ± 12.54	<65.91	10.75	1.25	10.17	J10233658+4220477
lk-259	163.53919	56.821007	0.0464892	444.33 ± 6.80	545.14 ± 10.77	293.35 ± 13.75	132.02 ± 16.50	62.02 ± 12.72	10.65	4.87	9.98	J10233684+4221037
lk-049	158.95834	56.568207	0.0437173	88.81 ± 7.24	213.97 ± 9.91	133.30 ± 17.40	99.05 ± 18.54	<88.23	10.50	0.64	9.95	J10272950+0114490
lk-203	162.58281	56.347740	0.0683074	<32.69	56.70 ± 12.84	104.47 ± 23.80	83.08 ± 13.14	<50.25	10.92	<0.83	9.86	J10325316+5306536
lk-082	159.70738	57.004242	0.0725609	100.16 ± 7.13	145.67 ± 9.50	74.33 ± 8.73	<57.07	<66.15	11.07	2.74	9.79	J10332972+4404342
en1-046	242.37892	53.863384	0.0623371	92.44 ± 7.53	150.81 ± 9.32	<109.83	<63.50	<88.18	10.84	1.84	<9.81	J10333162+4404212
lk-311	163.57295	57.726276	0.0751972	<30.52	102.61 ± 10.27	109.41 ± 12.00	74.62 ± 16.78	58.92 ± 14.05	10.85	1.21	10.75	J10364274+5447356
lk-048	158.79388	56.524883	0.0648007	<35.42	<46.16	<97.36	<135.89	<100.23	10.72	<0.80	<9.79	J10392338+3904501
lk-210	164.78847	56.918480	0.0467608	116.47 ± 9.11	125.71 ± 11.82	104.12 ± 10.38	<59.94	<56.94	10.46	1.27	9.56	J10435053+0645466
lk-006	161.48135	59.154591	0.0443921	115.51 ± 7.66	144.93 ± 9.13	140.13 ± 21.92	97.94 ± 23.19	<71.20	10.46	1.26	10.04	J10435268+0645256
lk-294	158.20099	56.595795	0.0468146	125.28 ± 13.13	136.48 ± 23.07	129.06 ± 24.26	<125.81	<133.61	10.72	1.36	9.64	J10452478+3910298
lk-355	159.07225	57.611805	0.0734656	52.54 ± 7.38	93.05 ± 9.02	<70.37	<47.40	<54.86	10.71	1.52	<9.78	J10514450+5101303
egs-017	213.85736	52.332111	0.0738315	<22.04	<30.92	<44.65	<41.72	<61.61	10.84	<0.67	<9.62	J10595915+0857357
lk-217	164.84148	56.605415	0.0478231	437.11 ± 15.59	288.91 ± 20.60	180.96 ± 17.65	79.12 ± 16.90	<84.74	10.53	5.01	9.53	J11014364+5720336
lk-379	159.88892	58.362122	0.0711125	59.99 ± 7.35	47.98 ± 8.99	<78.01	<72.30	<51.81	10.99	1.61	<9.79	J11064944+4751119
lk-357	159.91113	57.933495	0.0743553	<32.79	61.94 ± 8.95	96.29 ± 10.65	60.19 ± 12.21	62.14 ± 11.12	11.12	0.76	10.73	J11065068+4751090
lk-030	162.42171	60.293438	0.0444752	130.94 ± 7.59	231.78 ± 12.74	192.14 ± 12.74	118.29 ± 13.71	<59.04	10.56	1.50	10.24	J11204657+0028142
lk-273	161.65997	56.893730	0.0739821	<28.15	<41.51	<39.40	<70.40	<62.29	10.74	<0.85	<9.57	J11204801+0028068
lk-235	163.38641	56.303272	0.0719963	<66.31	<78.02	<53.87	<54.18	<63.11	10.63	<1.82	<9.66	J11251704+0227007

Table 4
(Continued)

(1) Galaxy ID (Control)	(2) R.A. (J2000)	(3) decl. (J2000)	(4) z redshift	(5) F100 μm (mJy)	(6) F160 μm (mJy)	(7) F250 μm (mJy)	(8) F350 μm (mJy)	(9) F500 μm (mJy)	(10) log $M_{\rm star}$ (log $M_{\odot}$)	(11) SFR ($M_{\odot}$ yr^{-1})	(12) log $M_{\rm gas}$ (log $M_{\odot}$)	(13) Galaxy ID (Pair)
lk-403	159.10716	58.556229	0.0271570	448.17 ± 14.58	844.33 ± 19.78	562.00 ± 34.14	335.35 ± 44.40	223.49 ± 32.19	10.88	1.87	10.33	J11251716+0226488
lk-200	162.21944	56.336193	0.0457280	272.88 ± 8.58	445.66 ± 12.10	232.15 ± 10.65	120.48 ± 13.54	64.99 ± 13.83	10.77	1.86	9.94	J11273289+3604168
lk-411	164.21436	59.534958	0.0564417	271.46 ± 9.06	394.70 ± 15.80	233.74 ± 20.27	136.18 ± 25.48	<104.61	11.10	3.99	10.19	J11273467+3603470
egs-005	213.76653	52.056580	0.0730016	140.23 ± 6.04	237.95 ± 7.26	124.57 ± 9.91	<54.80	<64.39	10.76	3.82	9.98	J11375801+4728143
egs-064	215.64249	53.585861	0.0391728	<23.97	<26.64	65.03 ± 14.33	67.53 ± 14.67	<56.35	10.30	<0.20	9.25	J11440433+3332339
lk-143	161.00293	58.760281	0.0727644	409.63 ± 7.16	501.07 ± 9.47	266.59 ± 9.86	128.54 ± 8.99	<54.95	10.84	9.91	10.25	J11484370+3547002
lk-054	160.78687	56.820522	0.0669273	52.30 ± 6.56	79.20 ± 10.29	42.51 ± 9.46	<41.99	<61.66	11.25	1.25	9.52	J11484525+3547092
lk-257	162.54466	56.727203	0.0480569	29.78 ± 6.97	82.68 ± 9.78	<52.06	<56.41	<38.82	10.76	0.37	<9.33	J11501333+3746107
lk-196	161.76175	56.254833	0.0460456	47.67 ± 8.59	<48.78	<46.06	<40.77	<72.34	10.87	0.52	<9.25	J11501399+3746306
en1-024	242.69853	53.422432	0.0630939	63.42 ± 14.58	116.81 ± 26.63	<51.28	<49.94	<41.89	10.78	1.32	<9.54	J11505764+1444200
lk-396	164.28052	59.031815	0.0738622	81.36 ± 8.56	143.36 ± 10.04	122.00 ± 11.69	82.89 ± 14.02	<77.19	10.87	3.08	10.57	J11542299+4932509
lk-267	161.13715	56.678345	0.0671536	493.37 ± 7.34	454.31 ± 10.58	224.42 ± 9.07	97.70 ± 14.05	<49.95	10.79	12.11	9.99	J12020424+5342317
lk-306	162.71820	57.585117	0.0268691	188.75 ± 6.88	194.89 ± 9.89	116.89 ± 12.05	69.83 ± 9.63	<53.31	10.29	0.69	9.21	J12054066+0135365
egs-050	216.14351	53.639969	0.0305066	556.26 ± 5.28	635.53 ± 7.29	289.99 ± 14.49	133.67 ± 13.69	<67.75	10.48	1.35	9.48	J12115507+4039182
egs-066	215.92018	53.915695	0.0337332	158.61 ± 6.09	297.18 ± 8.51	184.69 ± 16.18	113.68 ± 16.65	<56.01	10.46	0.61	9.73	J12115648+4039184
lk-007	162.01831	59.344875	0.0285956	35.20 ± 7.66	<38.28	<73.25	<112.69	<97.98	10.18	0.15	<9.06	J12191866+1201054
lk-334	160.10893	57.439854	0.0471860	156.15 ± 6.90	200.26 ± 9.94	118.32 ± 13.26	64.13 ± 12.23	<51.23	10.78	1.84	9.73	J12433887+4405399
lk-406	159.30702	58.571445	0.0710580	<29.39	72.43 ± 8.91	<77.49	<70.40	<64.35	10.97	<0.82	<9.78	J12525011+4645272
lk-079	158.74356	56.912376	0.0467561	50.86 ± 8.57	83.89 ± 9.61	<86.29	<74.66	<110.59	10.41	0.58	<9.49	J13011662+4803366
en1-015	241.90225	53.958252	0.0297046	500.88 ± 10.97	563.42 ± 14.85	262.97 ± 19.24	107.80 ± 24.03	<89.74	10.39	1.33	9.37	J13011835+4803304
lk-242	160.95529	56.281364	0.0240286	162.87 ± 6.55	107.87 ± 10.17	71.16 ± 13.78	<51.34	<57.17	9.71	0.46	8.92	J13082737+0422125
lk-015	161.59250	59.595676	0.0309583	<26.33	87.37 ± 9.83	<63.95	<54.83	<54.81	10.28	<0.13	<9.07	J13082964+0422045
btsh-094	216.88402	34.510860	0.0684431	56.61 ± 7.59	144.69 ± 10.43	118.59 ± 13.21	78.80 ± 19.06	<68.62	10.83	1.41	9.91	J13131470+3910382
en1-003	240.67156	54.337185	0.0653331	<42.65	<58.05	<53.20	<58.65	<74.50	10.69	<0.98	<9.58	J13151386+4424264
btsh-049	218.32701	34.734619	0.0343026	160.07 ± 6.58	259.88 ± 8.81	142.83 ± 9.14	70.35 ± 11.08	<55.22	10.97	0.62	9.46	J13151726+4424255
lk-035	159.37373	60.002872	0.0281504	657.91 ± 30.36	1118.77 ± 39.53	552.61 ± 31.50	261.23 ± 35.17	<179.53	10.71	1.66	9.89	J13153076+6207447
egs-040	214.24640	52.730427	0.0742157	<18.28	<24.81	<43.90	<60.95	<57.34	10.84	<0.57	<9.61	J13153506+6207287
lk-332	159.63516	57.400383	0.0470770	132.21 ± 7.70	101.67 ± 9.57	85.55 ± 13.16	<65.46	<53.79	10.67	1.45	9.49	J13325525–0301347
lk-279	163.63444	57.159027	0.0676157	170.72 ± 7.05	132.56 ± 10.32	69.30 ± 14.74	<69.46	<64.70	10.81	3.92	9.70	J13325655–0301395
lk-127	161.54971	58.449306	0.0496845	81.77 ± 6.99	126.44 ± 9.94	96.08 ± 8.88	63.09 ± 9.53	<59.96	10.72	1.19	10.02	J13462001–0325407
btsh-063	217.60631	35.321106	0.0104899	7971.50 ± 34.10	10153.50 ± 49.49	4483.15 ± 51.59	2000.98 ± 40.83	778.11 ± 50.94	10.69	2.69	9.80	J14003661–0254327
lk-078	158.71724	56.837643	0.0438288	112.75 ± 7.45	134.45 ± 9.45	104.62 ± 19.58	<72.55	<73.73	10.62	1.07	9.51	J14003796–0254227
btsh-123	217.08795	35.405602	0.0292952	271.58 ± 13.39	417.54 ± 12.38	285.34 ± 16.88	143.71 ± 17.97	<84.96	10.73	1.06	9.76	J14005783+4251203
lk-338	160.79364	57.647472	0.0467886	161.47 ± 7.16	237.07 ± 9.62	165.98 ± 10.06	66.66 ± 13.05	<90.31	10.57	1.46	9.79	J14005879+4250427
lk-130	163.01991	58.599899	0.0317531	54.19 ± 6.54	54.17 ± 8.89	85.58 ± 9.70	64.20 ± 12.10	<50.77	10.32	0.34	9.78	J14055079+6542598
lk-409	161.11449	58.903076	0.0312686	185.49 ± 7.64	266.49 ± 10.36	177.81 ± 9.91	93.54 ± 14.95	<55.48	10.15	0.92	9.65	J14062157+5043303
lk-170	161.25214	59.736507	0.0443880	74.04 ± 6.60	130.72 ± 8.45	93.14 ± 9.62	<60.19	<55.10	10.91	0.74	9.48	J14070703–0234513
lk-119	159.54161	58.017307	0.0237380	77.94 ± 6.04	153.66 ± 10.70	97.03 ± 11.75	76.17 ± 17.04	<68.58	10.05	0.15	9.25	J14234238+3400324
btsh-004	217.07809	34.284489	0.0333809	178.35 ± 7.68	213.48 ± 9.38	134.03 ± 7.29	72.16 ± 9.97	<54.91	10.06	1.15	9.51	J14234632+3401012
lk-270	161.44302	56.836800	0.0726175	<27.74	<40.26	<46.23	<57.17	<65.56	10.82	<0.81	<9.62	J14245831–0303597
lk-140	159.77400	58.361572	0.0733310	60.41 ± 7.80	186.05 ± 11.47	140.70 ± 10.95	72.19 ± 11.29	<53.95	11.07	1.67	10.37	J14245913–0304012
lk-321	158.19514	57.005798	0.0435024	95.40 ± 7.95	185.53 ± 10.26	<163.27	<116.77	<120.75	10.39	0.90	<9.67	J14250739+0313560
lk-383	160.20712	58.256981	0.0744073	<30.14	<39.98	<57.00	<72.24	<58.32	10.87	<0.92	<9.71	J14294766+3534275
lk-221	164.12077	56.910526	0.0469288	33.46 ± 7.51	129.71 ± 9.38	95.80 ± 10.13	<53.62	<93.02	10.57	0.39	9.53	J14295031+3534122
lk-245	161.70120	56.567902	0.0449944	49.80 ± 7.16	82.05 ± 10.14	65.79 ± 9.69	<53.06	<48.52	10.85	0.52	9.36	J14334683+4004512
lk-115	161.89583	58.101940	0.0742169	<33.16	<41.34	<74.73	<70.31	<57.00	10.86	<1.01	<9.81	J14334840+4005392
lk-055	161.28499	56.976227	0.0722381	175.59 ± 6.84	211.69 ± 9.60	114.39 ± 7.90	<50.18	<83.80	10.71	4.63	9.94	J14442055+1207429
egs-006	213.82188	51.831017	0.0745795	46.67 ± 5.32	54.83 ± 7.23	72.37 ± 10.70	<94.89	<61.91	11.06	1.41	9.80	J14442079+1207552
btsh-110	217.33472	34.753334	0.0688272	63.96 ± 6.98	78.00 ± 9.44	79.16 ± 8.47	<45.69	<64.54	10.68	1.60	9.77	J15002500+4317131
lk-156	158.50607	58.807034	0.0739712	<31.01	<41.82	<49.94	<48.82	<72.75	10.94	<0.94	<9.66	J15053137+3427534
lk-392	161.18837	58.454979	0.0313002	711.58 ± 15.32	1074.62 ± 19.74	690.00 ± 22.86	386.12 ± 25.36	193.31 ± 24.17	10.84	3.94	10.37	J15064391+0346364

Table 4
(Continued)

(1) Galaxy ID (Control)	(2) R.A. (J2000)	(3) decl. (J2000)	(4) z redshift	(5) F100 μm (mJy)	(6) F160 μm (mJy)	(7) F250 μm (mJy)	(8) F350 μm (mJy)	(9) F500 μm (mJy)	(10) log $M_{\rm star}$ (log $M_{\odot}$)	(11) SFR ($M_{\odot}$ yr^{-1})	(12) log $M_{\rm gas}$ (log $M_{\odot}$)	(13) Galaxy ID (Pair)
btsh-200	217.19626	33.387711	0.0424442	817.96 ± 19.21	767.78 ± 21.78	376.05 ± 9.11	159.56 ± 12.17	46.20 ± 10.36	10.77	5.92	9.78	J15064579+0346214
btsh-102	218.83510	33.846039	0.0581498	168.61 ± 6.19	209.07 ± 8.98	127.37 ± 14.89	67.08 ± 16.65	54.19 ± 13.48	10.68	2.82	9.80	J15101587+5810425
lk-365	162.09343	58.195721	0.0465291	37.22 ± 7.18	138.01 ± 9.67	89.73 ± 15.62	48.23 ± 10.88	<58.27	10.49	0.45	9.90	J15101776+5810375
egs-044	214.52928	52.697277	0.0659781	61.25 ± 5.59	95.40 ± 8.69	<47.40	<50.54	<63.38	10.73	1.40	<9.55	J15144544+0403587
lk-169	159.02901	59.379044	0.0732209	104.47 ± 7.13	168.32 ± 8.29	80.07 ± 13.21	<51.76	<60.20	10.67	2.91	9.82	J15144697+0403576
btsh-050	218.26311	34.744881	0.0296272	75.02 ± 8.03	187.08 ± 10.74	190.83 ± 7.02	113.02 ± 14.13	54.16 ± 11.13	10.14	0.40	9.97	J15233768+3749030
lk-091	163.20827	57.747452	0.0730649	175.22 ± 7.75	151.40 ± 9.59	77.31 ± 9.95	51.25 ± 11.66	<36.18	10.70	5.03	9.61	J15264774+5915464
lk-106	159.34660	57.520683	0.0718920	397.72 ± 7.14	376.18 ± 10.43	168.52 ± 16.53	<64.12	<61.08	10.87	9.96	10.07	J15281276+4255474
lk-164	163.10425	59.685532	0.0277227	1146.73 ± 12.16	1605.01 ± 17.47	875.35 ± 19.63	416.53 ± 35.14	132.22 ± 26.56	10.74	2.78	9.99	J15281667+4256384
lk-269	161.45438	56.701805	0.0672907	57.40 ± 6.92	103.00 ± 8.95	48.54 ± 10.61	<54.29	<58.99	10.84	1.38	9.57	J15523393+4620237
lk-146	162.65512	59.095657	0.0323721	290.86 ± 7.64	259.00 ± 10.45	145.66 ± 13.88	<64.38	<61.28	10.22	1.43	9.40	J15562191+4757172
lk-040	162.04411	56.704330	0.0477595	74.63 ± 6.81	125.26 ± 10.66	74.89 ± 7.77	<37.45	<47.58	10.48	0.87	9.46	J15583749+3227379
lk-028	161.42595	60.067890	0.0719979	53.20 ± 7.18	103.07 ± 11.01	71.96 ± 10.60	<53.86	<68.80	10.79	1.48	9.77	J15583784+3227471
egs-026	213.78456	51.613804	0.0742349	244.41 ± 10.83	287.85 ± 12.13	127.77 ± 14.48	<71.02	<62.44	10.75	6.71	10.00	J16024254+4111499
lk-224	165.37244	57.117775	0.0451835	303.19 ± 7.74	467.53 ± 12.26	229.45 ± 9.54	108.68 ± 9.88	<60.84	10.58	1.97	9.84	J16024475+4111589
lk-366	162.32683	58.345104	0.0280867	78.43 ± 8.30	237.33 ± 9.72	215.25 ± 10.28	112.63 ± 13.33	<87.83	10.81	0.32	9.87	J16080559+2529091
lk-281	164.13226	57.347748	0.0675492	51.07 ± 7.74	127.73 ± 9.47	120.37 ± 12.37	65.86 ± 13.76	<75.45	11.11	1.06	10.31	J16080648+2529066
btsh-028	218.14639	34.364929	0.0422711	30.39 ± 6.33	68.86 ± 8.07	57.41 ± 9.14	<53.69	<70.53	10.47	0.29	9.27	J16082261+2328459
lk-345	162.32899	57.821774	0.0702557	128.20 ± 7.22	176.90 ± 9.49	66.96 ± 13.36	<68.14	<53.16	10.57	3.23	9.72	J16082354+2328240
lk-387	160.41603	58.317230	0.0722775	65.57 ± 6.61	96.26 ± 10.94	84.75 ± 12.78	<63.62	<61.34	11.10	1.82	9.83	J16145418+3711064
lk-243	161.15924	56.369724	0.0240542	1293.33 ± 11.99	1304.87 ± 16.83	588.23 ± 21.66	286.68 ± 21.50	<135.42	10.81	3.66	9.63	J16282497+4110064
lk-139	159.74431	58.376003	0.0679610	172.97 ± 7.39	165.39 ± 9.12	84.48 ± 10.98	62.33 ± 12.82	<97.77	10.74	4.14	9.73	J16282756+4109395
lk-278	163.33688	57.242729	0.0802541	75.46 ± 6.70	91.48 ± 8.92	53.06 ± 13.16	<71.33	<54.35	11.19	2.60	9.75	J16354293+2630494
egs-038	213.91566	52.543880	0.0737351	61.64 ± 5.41	143.09 ± 7.66	164.18 ± 11.88	66.53 ± 14.99	<48.53	11.29	2.04	10.52	J16372583+4650161
lk-227	162.26764	56.223995	0.0719589	549.85 ± 8.26	538.53 ± 11.64	269.88 ± 10.05	115.67 ± 12.98	61.87 ± 10.89	10.90	15.46	10.19	J16372754+4650054
en1-041	241.28255	54.887733	0.0632211	<27.27	<45.90	58.78 ± 14.37	<54.11	<113.47	10.60	<0.60	9.59	J17020378+1859495
lk-122	160.10104	58.155136	0.0720025	174.47 ± 6.81	321.35 ± 10.52	175.95 ± 9.86	73.90 ± 15.11	<55.78	10.72	3.16	10.17	J17045089+3448530
lk-376	159.78526	58.231022	0.0729322	57.36 ± 7.32	<45.37	83.03 ± 8.45	<68.12	<66.86	10.90	1.63	9.83	J17045097+3449020
lk-240	160.43297	56.250572	0.0704346	58.85 ± 6.97	80.12 ± 9.71	64.40 ± 11.86	<43.86	<55.05	10.98	1.55	9.71	J20471908+0019150

Note. Descriptions of Columns: (1) Control Galaxy ID. (2) Control Galaxy R.A. (deg, J2000). (3) Control Galaxy decl. (deg, J2000). (4) Control Galaxy redshift z taken from SDSS. (5) *Herschel* PACS 100 μm flux (mJy). (6) *Herschel* PACS 160 μm flux (mJy). (7) *Herschel* SPIRE 250 μm flux (mJy). (8) *Herschel* SPIRE 350 μm flux (mJy). (9) *Herschel* SPIRE 500 μm flux (mJy). (10) Stellar mass (log($M_{\odot}$)). (11) Star formation rate ($M_{\odot}$ yr^{-1}). (12) Total gas mass (log($M_{\odot}$)). (13) ID of matched H-KPAIR galaxy.

(This table is available in machine-readable form.)

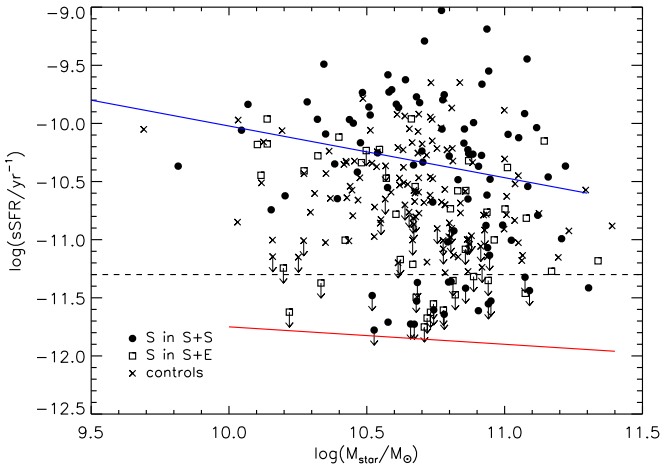

Figure 7. Stellar mass ($M_{\rm star}$) vs. sSFR scatter plot, for S in S+S (filled circles) and S+E (open squares) pairs, and control samples (crosses). The blue and red lines represent the blue and red sequences, taken from Schiminovich et al. (2007).

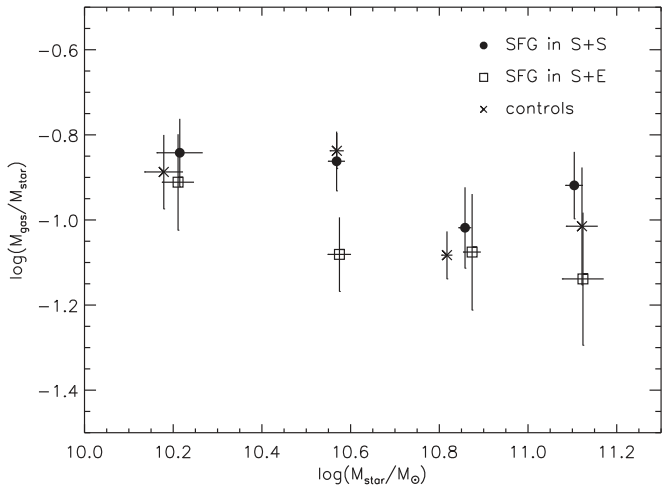

Figure 9. Plot of means of $\log(M_{\rm gas}/M_{\rm star})$ in four stellar mass ($M_{\rm star}$) bins for SFGs in S+S (filled circles) and S+E (open squares) pairs, and control samples (crosses).

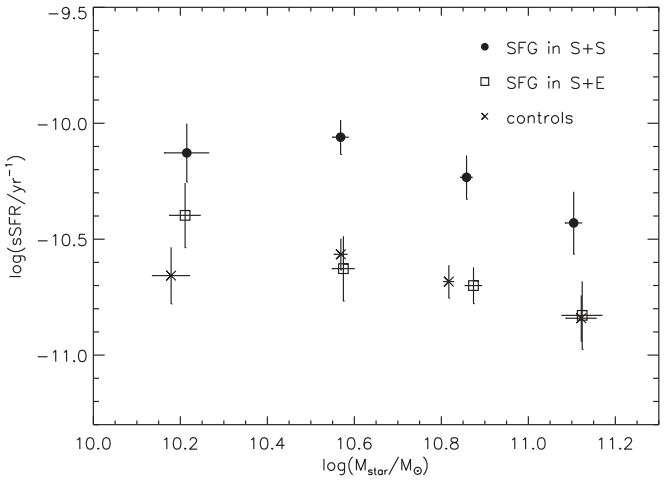

Figure 8. Plot of the mean values of sSFRs in four stellar mass ($M_{\rm star}$) bins: for SFGs in S+S (black filled circles) and S+E (open squares) pairs, and control samples (crosses).

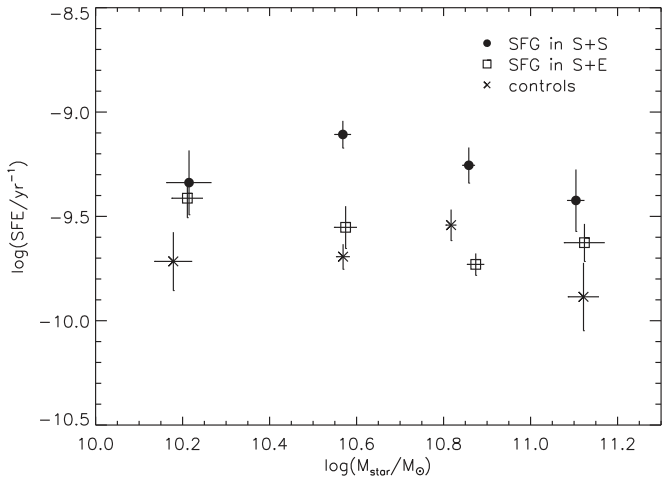

Figure 10. Statistical comparison of star formation efficiencies (SFE = SFR/$M_{\rm gas}$) in four stellar mass ($M_{\rm star}$) bins for SFGs in S+S (filled circles) and S+E (open squares) pairs, and control samples (crosses).

7. STAR FORMATION EFFICIENCY ENHANCEMENT

According to James et al. (2002) the total gas mass ($M_{\rm gas}$) can be estimated from $M_{\rm dust}$: $M_{\rm gas}/M_{\rm dust} = 1/(Z \times e \times f) = 114/Z$, where Z is the metallicity in solar units, $e = 0.456$ is the fraction of metals incorporated in dust in the ISM, and $f = 0.019$ is the metal mass fraction in gas of solar metallicity. Draine et al. (2007) found a very similar gas-to-dust ratio ($M_{\rm gas}/M_{\rm dust}$ ~100) for SINGS galaxies, including interacting galaxies. Studies on gas-to-dust mass ratios in local galaxies (e.g., Rémy-Ruyer et al. 2014) show that for metal-rich galaxies the ratios are uniformally distributed, and only very metal-poor galaxies have significantly higher $M_{\rm gas}/M_{\rm dust}$ ratios. In the local universe, only low-mass galaxies have such low metallicities (Tremonti et al. 2004). All SFGs in H-KPAIR have $M_{\rm star} > 10^{9.8} M_\odot$, and the control galaxies are 1-to-1 matched to paired galaxies according to $M_{\rm star}$. Therefore we adopted a fixed gas-to-dust ratio of 100 for the conversion from $M_{\rm dust}$ to $M_{\rm gas}$. Using the K–M estimator, we found that the means of $\log(M_{\rm gas}/M_{\rm star})$ of SFGs in S+S pairs, in S+E pairs, and in the control sample are -0.93 ± 0.05, -1.07 ± 0.07, and -1.00 ± 0.04, respectively. For both SFGs in S+S pairs and in S+E pairs, the mean $\log(M_{\rm gas}/M_{\rm star})$ differs from that of control galaxies only at a $\sim 1\sigma$ level. In Figure 9 the means of $\log(M_{\rm gas}/M_{\rm star})$ of different samples in different mass bins are compared. No clear trend is found in the plot.

The SFE is defined as the ratio between the SFR and total gas mass: SFE = SFR/$M_{\rm gas}$. The SFE analysis was confined to SFGs with $M_{\rm gas}$ detections. The means of $\log({\rm SFE/yr^{-1}})$ of SFGs in S+S pairs, in S+E pairs, and in the control sample are found to be -9.26 ± 0.05, -9.56 ± 0.05, and -9.67 ± 0.05, respectively. Figure 10 shows that the means of log(SFE) of SFGs in S+S pairs are consistently above that of control galaxies at a ~0.4 dex level in all mass bins. On the other hand, the means of log(SFE) of SFGs in S+E pairs are seen both above and below that of control galaxies, consistent with no significant SFE enhancement.

In Figure 11 we plotted the mean log(SFE) against the gas fraction $f_{\rm gas} = M_{\rm gas}/(M_{\rm star} + M_{\rm gas})$ for the S+S pair and control samples. Within the range of $f_{\rm gas}$ covered by SFGs in our samples, which is [0, 0.25], there is no significant dependence of the SFE enhancement on $f_{\rm gas}$. Taken at the face

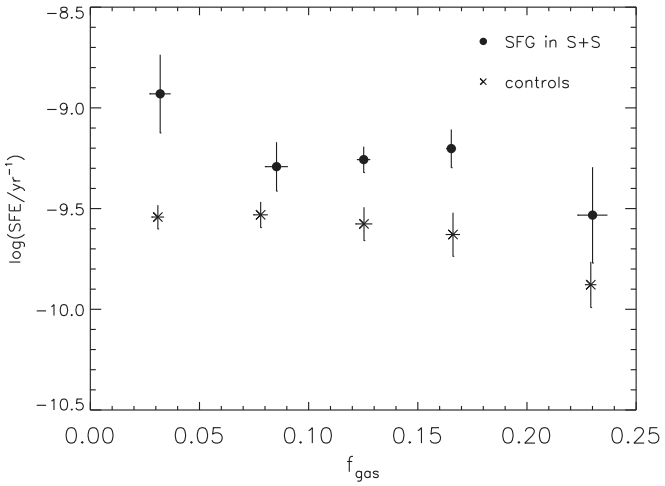

Figure 11. Statistical comparison of SFEs in five gas mass fraction ($f_{gas} = M_{gas}/(M_{gas} + M_{star})$) bins, for SFGs in S+S pairs (filled circles) and control samples (crosses).

value, this does not confirm the results of theoretical simulations showing weaker merger-induced star formation enhancement for high f_{gas} (Hopkins et al. 2009; Perret et al. 2014; Scudder et al. 2015). However, it appears that the effect of f_{gas} on star formation enhancement is significant only when $f_{gas} \gtrsim 0.3$ (Scudder et al. 2015), which is beyond the range covered by our samples.

8. DISCUSSION

8.1. AGNs in H-KPAIR

In the H-KPAIR sample, some spiral galaxies are classified as AGNs based on their optical spectra. J08364588+4722100, J11251716+0226488, J11484525+3547092, J13151386+4424264, J13325655−0301395, J14234632+3401012, J14294766+3534275, J15281276+4255474, and J20471908+0019150 are sub-classified (SUBCLASS) as AGNs or AGN Broadline in the SDSS archive (using line ratios). J09134606+4742001 and J13151726+4424255 are classified as AGNs in "Quasars and AGNs" (13th Ed.; Véron-Cetty & Véron 2010). J13462001−0325407 is classified as Sy2 in Véron-Cetty & Véron (2010).

The identification of AGNs has been successful through the use of *WISE* photometry (Jarrett et al. 2011; Stern et al. 2012; Mateos et al. 2012; Secrest et al. 2015). To apply the corresponding AGN color criteria of Mateos et al. (2012), the W1, W2, and W3 magnitudes are taken from the unWISE forced photometry catalog (Lang et al. 2014; Lang 2014). The catalog apertures are chosen from SDSS photometry and are held constant for each identified object across the three *WISE* bands. The forced photometry should be sufficient to measure the magnitude differences W1–W2 and W2–W3 for the placement of the H-KPAIRs in the *WISE* color–color diagram. A comparison to manual aperture photometry is examined in Domingue et al. (2015, in preparation). From the full set of spirals in the H-KPAIRs, only J13151726+4424255 falls within the color–color diagram area associated with AGNs in Mateos et al. (2012) and therefore this may be our only AGN candidate in addition to the optically determined AGNs. More details on discussions on *WISE* AGNs will be in D. Domingue et al. (2015, in preparation).

Table 5
sSFR and SFE Enhancement

(1) Type	(2) sSFR Enhancement (dex)	(3) SFE Enhancement (dex)	4 $\delta \log(M_{gas}/M_{star})$ (dex)
S in S+S	0.46 ± 0.08	0.41 ± 0.07	0.07 ± 0.06
S in S+E	0.03 ± 0.08	0.11 ± 0.07	−0.07 ± 0.08

Note. Mean values of sSFR and SFE enhancements (dex) and of the difference in $\log(M_{gas}/M_{star})$, for SFGs in S+S and S+E pairs.

Lam et al. (2013) found that the FIR/submillimeter properties of galaxies with AGNs are similar to those of star-forming galaxies, and the AGN contribution to the FIR/submillimeter luminosity is in general insignificant. Even in the MIR band where the AGN contribution is much stronger, Nordon et al. (2012) found that only in 2 out of 18 AGN-hosting galaxies is the emission significantly enhanced by the AGN. Therefore, differing from Xu et al. (2010), we choose to keep the AGN candidates in our analyses. Indeed we found that keeping or removing AGN candidates will not affect the major results of this paper.

8.2. Why is SFR Enhancement Absent in S+E Pairs?

The significant sSFR enhancements of SFGs in S+S pairs found in Xu et al. (2010) and in this work are due to a significant SFE enhancement within them, while they have the same mean gas content as the control galaxies. On the other hand, the lack of sSFR enhancement in SFGs in S+E pairs cannot be attributed to a deficiency of gas content, as speculated by Xu et al. (2010), but to a significantly lower SFE than that of SFGS in S+S pairs (Table 5). It is difficult to understand the SFE difference between SFGs in S+S pairs and those in S+E pairs, if the enhancement is triggered by tidal effects (the tidal effects caused by a spiral companion and by a elliptical companion should be similar). It has been suggested that cloud-cloud collisions (Scoville et al. 1986; Tan et al. 2006) or cloud-squeezing by shock-heated diffuse gas in two colliding disks (Jog & Solomon 1992; Saitoh et al. 2009; Hayward et al. 2014; Renaud et al. 2015) can trigger starbursts. Our results indicate that these mechanisms, associated with the collision between the ISM in two gas-rich galaxies (which is absent in S+E pairs), may indeed be the major mode for the SFR enhancement in paired SFGs (mostly early-stage mergers). Hwang et al. (2011) also found that in the GOODS-*Herschel* fields the SFR and sSFR increase as a late-type galaxy approaches a late-type neighbor (S+S pairs), while the SFR and sSFR decrease or do not change much as the galaxy approaches an early-type neighbor (S+E pairs). They argued for X-rays from the ellipticals as the reason for the suppression of star formations in the spirals in S+E pairs.

8.3. Separation and SFR Enhancement

In Section 5.7 of Xu et al. (2010), they discussed how the star formation enhancement is related to the projected separation between the two galaxies in pairs. Here we made a similar analysis using the normalized separation parameter: $\mathrm{SEP} = s/(r1+r2)$. Here s is the projected separation, and $r1$ and $r2$ are the K-band Kron radii (taken from 2MASS) of the primary and the secondary, respectively, in the same units as those of s (arcsec). Figures 12 and 13 are plots of mean log

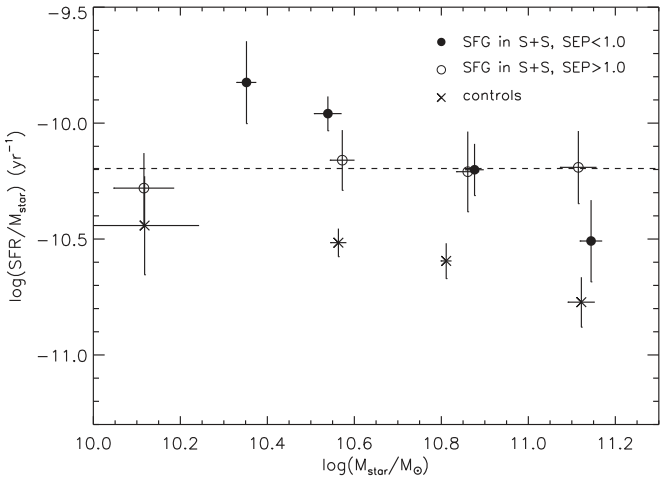

Figure 12. Similar to Figure 17 in Xu et al. (2010), average sSFRs of SFGs in S+S pairs, separated into two subsamples of SEP < 1 (filled dots) and SEP > 1 (opened circles), respectively. The dotted line marks the mean log(SFR/$M_{\rm star}$) of all SFGs in the H-KPAIR sample.

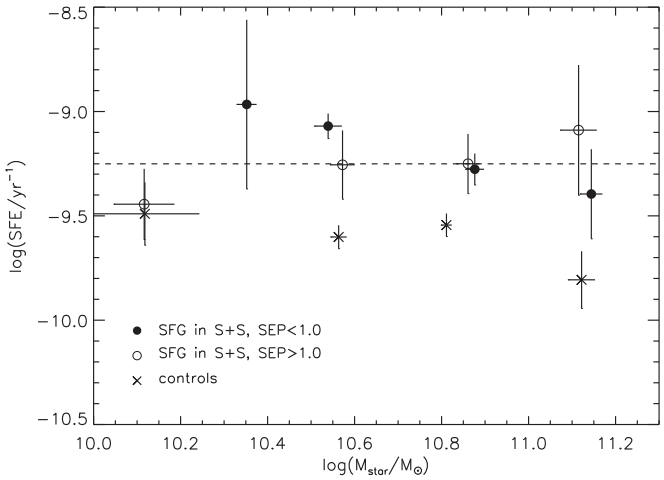

Figure 13. Average log(SFE) (SFR/$M_{\rm gas}$) of SFGs in S+S pairs, separated into two subsamples of SEP < 1 (filled dots) and SEP > 1 (opened circles), respectively. The dotted line marks the mean log(SFR/$M_{\rm gas}$) of all SFGs in the H-KPAIR sample.

(SFR/$M_{\rm star}$) and log(SFR/$M_{\rm gas}$) versus log($M_{\rm star}$) of star-forming spirals (SFGs) in S+S pairs, separated into two subsamples of SEP < 1 (39 SFGs) and SEP > 1 (30 SFGs). Similar to Xu et al. (2010), for both subsamples we found that the log(SFR/$M_{\rm star}$) and log(SFR/$M_{\rm gas}$) versus log($M_{\rm star}$) relations scatter around the means of the total sample without any obvious trend, and no significant differences between the two subsamples are detected. This confirms Xu et al.'s (2010) finding and suggests that for early-stage mergers in H-KPAIR, the separation is not an important parameter anymore once the two galaxies are close enough. This is different from FIR-selected late-stage mergers for which Gao & Solomon (1999) found an anti-correlation between SFE and the pair separation.

8.4. "Holmberg Effect"

Figure 14 shows a correlation between the sSFR of primary galaxies and that of secondary galaxies in S+S pairs with the Spearman's rank correlation coefficient equal to 0.56, while for corresponding control galaxies there is no such correlation. This reconfirms the "Holmberg effect" on the sSFR previously found by Xu et al. (2010) using *Spitzer* observations of a small subsample of KPAIR.

9. SUMMARY AND FUTURE PLAN

In this paper we present *Herschel* observations for a large and complete sample of close major-merger pairs of galaxies selected from a 2MASS/SDSS-DR5 cross-match. The H-KPAIR sample includes 176 galaxies (132 spirals and 44 ellipticals) in 88 pairs (44 S+S and 44 S+E). *Herschel* maps, in the 3 PACS bands at 70, 100 and 160 μm and the three SPIRE bands at 250, 350 and 500 μm, show very diversified FIR-submillimeter emission properties among H-KPAIR galaxies. The SFR (estimated using the IR luminosity), the sSFR, the total gas mass $M_{\rm gas}$ (estimated using the SED fitting resulted dust mass), and the SFE of the spiral galaxies in H-KPAIR are compared to those of single spirals in a control sample in order to study the interaction-induced enhancement. The control sample is selected from 2MASS galaxies with *Herschel* data obtained in HerMES Level-5 surveys. In order to minimize a bias due to different depths of the *Herschel* data of

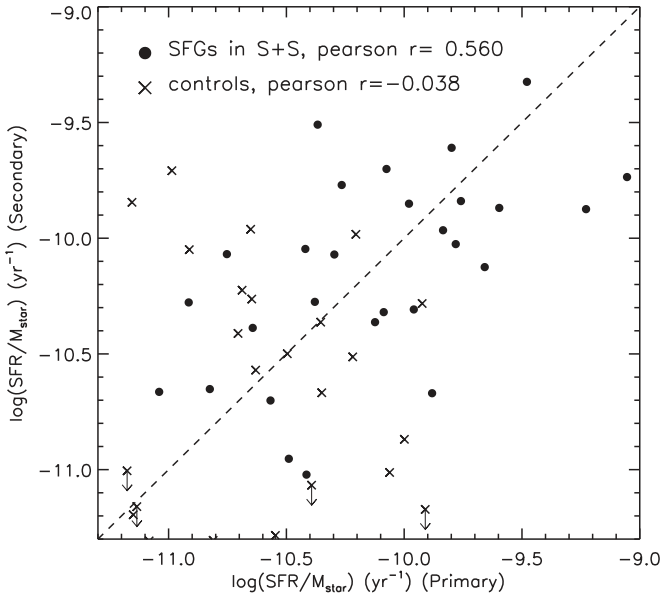

Figure 14. Plot of sSFRs of primary and secondary star-forming spiral galaxies in S+S pairs (filled circles) and control samples (crosses).

H-KPAIR and of the control sample, the enhancement analyses are confined to SFGs with log(sSFR/yr^{-1}) > -11.3. The following results are found.

1. The mean log(sSFR) of the SFGs in S+S pairs is significantly higher than that of the SFGs in the control sample, but that of SFGs in the S+E pairs is not. The sSFR enhancement level for SFGs in S+S pairs is ~0.5 dex. This result is in very good agreement with Xu et al. (2010).
2. SFGs in S+S pairs of INT and MER types have enhancement of log(sSFR) (by 0.17 dex) above those in JUS pairs, though the significance of the difference is only at the 1.5σ level. No significant sSFR enhancement is found for SFGs in S+E pairs of either the INT/MER types or the JUS type.
3. There is no significant difference among the means of log($M_{\rm gas}/M_{\rm star}$) of SFGs in S+S pairs, in S+E pairs, and in the control sample.

4. The mean log(SFE) of the SFGs in S+S pairs is higher than those of the SFGs in S+E pairs and in the control sample. This indicates that star formation triggered by disk–disk collision may play an important role in the interaction-induced star formation activity.
5. There is no dependence of the SFE enhancement on the gas fraction, $f_{\rm gas}$, in the range of $f_{\rm gas}$ of our sample ($0 < f_{\rm gas} < 0.25$).

In future works we will study the atomic and molecular gas contents in H-KPAIR galaxies using GBT HI and IRAM-30 m CO observations (U. Lisenfeld et al. 2015, in preparation). Using *WISE* mid-infrared images, we will analyze the PAH properties and AGN activities of paired galaxies (D. Domingue et al. 2015, in preparation). Analysis on the stellar populations and metallicity gradients in paired galaxies and detailed studies on SFGs in S+E pairs will be carried out by using optical spectroscopic observations with the 2.16 m telescope of the National Astronomical Observatory of China (NAOC), and narrowband H_α imaging observations with the 2.4 m telescope of the Yunnan Astronomical Observatory.

We thank the anonymous referee for helpful comments and suggestions. We acknowledge useful discussions with Dr. Yinghe Zhao, and thank Dr. Yuyen Chang for the help with data tables of 1 M galaxies from SDSS+*WISE*. C.C. and Y.G. are supported by NSFC-11503013, NSFC-11420101002, NSFC-10978014, NSFC-11173059, NSFC-11390373, and CAS-XDB09000000. U.L. acknowledges support by the research projects AYA2011-24728 and AYA2014-53506-P from the Spanish Ministerio de Economía y Competividad and the Junta de Andalucía (Spain). The *Herschel* spacecraft was designed, built, tested, and launched under a contract with ESA, managed by the *Herschel*/*Planck* Project team through an industrial consortium under the overall responsibility of the prime contractor Thales Alenia Space (Cannes), and including Astrium (Friedrichshafen), responsible for the payload module and for system testing at the spacecraft level, Thales Alenia Space (Turin), responsible for the service module, and Astrium (Toulouse) responsible for the telescope, with an excess of a hundred subcontractors. HCSS/HSpot/HIPE are joint developments by the *Herschel* Science Ground Segment Consortium, consisting of ESA, the NASA *Herschel* Science Center, and the HIFI, PACS and SPIRE consortia. This research has made use of the NASA/IPAC Extragalactic Database (NED), which is operated by the Jet Propulsion Laboratory, California Institute of Technology, under contract with the National Aeronautics and Space Administration.

REFERENCES

Alonso, M. S., Tissera, T. B., Coldwell, G., et al. 2004, MNRAS, 352, 1081
Bahcall, J. N., Kirhakos, S., & Schneider, D. P. 1995, ApJ, 450, 486
Barton, E. J., Geller, M. J., & Kenyon, S. J. 2000, ApJ, 530, 660
Bergvall, N., Laurikainen, E., & Aalto, S. 2003, A&A, 405, 31
Buat, V., & Xu, C. 1996, A&A, 306, 61
Bushouse, H., Lamb, S., & Werner, M. 1988, ApJ, 335, 74
Calzetti, D. 2013, in Star Formation Rate Indicators 2013, ed. J. Falcón-Barroso, & J. H. Knapen (Cambridge, UK: Cambridge University Press), 419
Chang, Y.-Y., van der Wel, A., da Cunha, E., & Rix, H.-W. 2015, ApJS, 219, 8
da Cunha, E., Charlot, S., & Elbaz, D. 2008, MNRAS, 388, 1595
Dale, D. A., Aniano, G., Engelbracht, C. W., et al. 2012, ApJ, 745, 95
Dale, D. A., Bendo, G. J., & Engelbracht, C. W. 2005, ApJ, 633, 857
Dasyra, K. M., Tacconi, L. J., Davies, R. I., et al. 2006, ApJ, 638, 745
Domingue, D. L., Sulentic, J. W., Xu, C., et al. 2003, AJ, 125, 555
Domingue, D. L., Xu, C. K., Jarrett, T. H., & Cheng, Y. 2009, ApJ, 695, 1559
Draine, B. T., Dale, D. A., Bendo, G., et al. 2007, ApJ, 663, 866
Draine, B. T., & Li, A. 2007, ApJ, 657, 810
Dunne, L., & Eales, S. A. 2001, MNRAS, 327, 697
Ellison, S. L., Patton, D. R., Simard, L., et al. 2008, AJ, 135, 1877
Erwin, P. 2015, ApJ, 799, 226
Feigelson, E. D., & Nelson, P. I. 1985, ApJ, 293, 192
Gao, Y., & Solomon, P. M. 1999, ApJL, 512, L99
Griffin, M. J., Abergel, A., Abreu, A., et al. 2010, A&A, 518, L3
Haynes, M., & Herter, T. 1988, AJ, 96, 504
Hayward, C. C., Lanz, L., Ashby, M. L. N., et al. 2014, MNRAS, 445, 1598
Hopkins, P. F., Cox, T. J., Younger, J. D., & Hernquist, L. 2009, ApJ, 691, 1168
Hopkins, P. F., Hernquist, L., Cox, T. J., et al. 2006, ApJS, 163, 1
Hwang, H. S., Elbaz, D., Dickinson, M., et al. 2011, A&A, 535, 60
James, A., Dunne, L., Eales, S., & Edmunds, M. G. 2002, MNRAS, 335, 753
Jarrett, T. H., Cohen, M., Masci, F., et al. 2011, ApJ, 735, 112
Jog, C. J., & Solomon, P. M. 1992, ApJ, 387, 152
Kaplan, E. L., & Meier, P. 1958, J. Am. Stat. Assoc., 53, 457
Kauffmann, G., Heckman, T. M., White, S. D. M., et al. 2003, MNRAS, 341, 33
Kennicutt, R. C. 1996, in Saas-Fee Advanced Course 26, Galaxies: Interactions and Induced Star Formation, ed. D. Friedli, L. Martinet, & D. Pfenniger (Berlin: Springer), 1
Kennicutt, R. C. 1998, ARA&A, 36, 189
Kennicutt, R. C., Keel, W., van der Hulst, J., et al. 1987, AJ, 93, 1001
Kormendy, J., & Kennicutt, R. C. 2004, ARA&A, 42, 603
Lam, M. I., Wu, H., Zhu, Y.-N., & Zhou, Z.-M. 2013, RAA, 13, 179
Lambas, D. G., Tissera, P. B., Alonso, M. S., & Coldwell, G. 2003, MNRAS, 346, 1189
Lang, D. 2014, AJ, 147, 108
Lang, D., Hogg, D. W., & Schlegel, D. J. 2014, arXiv:1410.7397
Lanz, L., Zezas, A., Brassington, N., et al. 2013, ApJ, 768, 90
Larson, R. B., & Tinsley, B. M. 1978, ApJ, 219, 46
Li, C., Kauffmann, G., Heckman, T. M., Jing, Y. P., & White, S. D. M. 2008, MNRAS, 385, 1903
Lintott, C., Schawinski, K., Bamford, S., et al. 2011, MNRAS, 410, 166
Mateos, S., Alonso-Herrero, A., Carrera, F. J., et al. 2012, MNRAS, 426, 3271
Mihos, J. C., & Hernquist, L. 1996, ApJ, 464, 641
Moon, J.-S., & Yoon, S.-J. 2015, PKAS, 30, 469
Nikolic, B., Cullen, H., & Alexander, P. 2004, MNRAS, 355, 874
Nordon, R., Lutz, D., Genzel, R., et al. 2012, ApJ, 745, 182
Oliver, S., Bock, J., Altieri, B., et al. 2012, MNRAS, 424, 1614
Ott, S. 2010, in ASP Conf. Ser. 434, Astronomical Data Analysis Software and Systems XIX, ed. Y. Mizumoto, K.-I. Morita, & M. Ohishi (San Francisco, CA: ASP), 139
Park, C., & Choi, Y.-Y. 2005, ApJL, 635, L29
Park, C., & Choi, Y.-Y. 2009, ApJ, 691, 1828
Park, C., Gott, J. R., III, & Choi, Y.-Y. 2008, ApJ, 674, 784
Patton, D. R., Torrey, P., Ellison, S. L., et al. 2013, MNRAS, 433, L59
Perret, V., Renaud, F., Epinat, B., et al. 2014, A&A, 562, A1
Poglitsch, A., Waelkens, C., Geis, N., et al. 2010, A&A, 518, L2
Rémy-Ruyer, A., Madden, S. C., Galliano, F., et al. 2014, A&A, 563, A31
Renaud, F., Bournaud, F., & Duc, P.-A. 2015, MNRAS, 446, 2038
Saitoh, T. R., Daisaka, H., Kokubo, E., et al. 2009, PASJ, 61, 481
Schiminovich, D., Wyder, T. K., Martin, D. C., et al. 2007, ApJS, 173, 315
Scoville, N., Aussel, H., Brusa, M., et al. 2007, ApJS, 172, 1
Scoville, N. Z., Sanders, D. B., & Clemens, D. P. 1986, ApJL, 310, L77
Scudder, J. M., Ellison, S. L., Momjian, E., et al. 2015, MNRAS, 449, 3719
Scudder, J. M., Ellison, S. L., Torrey, P., Patton, D. R., & Mendel, J. T. 2012, MNRAS, 426, 549
Secrest, N. J., Dudik, R. P., Dorland, B. N., et al. 2015, ApJS, 221, 12
Stern, D., Assef, R. J., Benford, D. J., et al. 2012, ApJ, 753, 30
Sulentic, J. 1989, AJ, 98, 2006
Surace, J. A., Sanders, D. B., Vacca, W. D., et al. 1998, ApJ, 492, 116
Tan, J. C., Krumholz, M. R., & McKee, C. F. 2006, ApJL, 641, L121
Telesco, C. M., Wolstencroft, R. D., & Done, C. 1988, ApJ, 329, 174
Toomre, A., & Toomre, M. 1972, ApJ, 178, 623
Traficante, A., Calzoletti, L., Veneziani, M., et al. 2011, MNRAS, 416, 2932
Tremonti, C. A., Heckman, T. M., Kauffmann, G., et al. 2004, ApJ, 613, 898
Véron-Cetty, M.-P., & Véron, P. 2010, A&A, 518, A10
Woods, D. F., & Geller, M. J. 2007, AJ, 134, 527
Xu, C., Hacking, P. B., Fang, F., et al. 1998, ApJ, 508, 576

Xu, C., & Sulentic, J. W. 1991, ApJ, 374, 407
Xu, C. K., Domingue, D., Cheng, Y., et al. 2010, ApJ, 713, 330
Xu, C. K., Shupe, D. L., Béthermin, M., et al. 2012a, ApJ, 760, 72
Xu, C. K., Sun, Y. C., & He, X. T. 2004, ApJL, 603, L73
Xu, C. K., Zhao, Y., Scoville, N., et al. 2012b, ApJ, 747, 85
Yuan, F.-T., Takeuchi, T. T., Matsuoka, Y., et al. 2012, A&A, 548, A117